Title:

Base editing of *Ptbp1* in neurons alleviates symptoms in a mouse model of Parkinson's disease

Authors:

Desirée Böck[1,#,*], Maria Wilhelm[1,#], Jonas Mumenthaler[1], Daniel Fabio Carpanese[1], Peter I. Kulcsár[1], Simon d'Aquin[1], Alessio Cremonesi[2], Anahita Rassi[2], Johannes Häberle[3], Tommaso Patriarchi[1,4*], Gerald Schwank[1,*]

[#]These authors contributed equally.

[*]Correspondence: patriarchi@pharma.uzh.ch; schwank@pharma.uzh.ch; desiree.boeck@uzh.ch

Affiliations:

[1]Institute of Pharmacology and Toxicology, University of Zurich, Zürich, Switzerland

[2]Division of Clinical Chemistry and Biochemistry, University Children's Hospital Zurich, University of Zurich, Zurich, Switzerland

[3]Division of Metabolism and Children's Research Center, University Children's Hospital Zurich, Zurich, Switzerland

[4]Neuroscience Center Zurich, University of Zurich and ETH Zurich, Zurich, Switzerland

Abstract

Parkinson's disease (PD) is a multifactorial disease caused by irreversible progressive loss of dopaminergic neurons (DANs). Recent studies have reported successful conversion of astrocytes into DANs by repressing polypyrimidine tract binding protein 1 (PTBP1), which led to the rescue of motor symptoms in a chemically-induced mouse model of PD. However, several follow-up studies have questioned the validity of this astrocyte to DAN conversion model. In this study, we devised an adenine base editing strategy to downregulate PTBP1 in astrocytes and neurons in a chemically-induced PD mouse model. While PTBP1 downregulation in astrocytes had no effect, we observed that PTBP1 downregulation in neurons of the substantia nigra pars compacta and striatum resulted in the expression of the DAN marker tyrosine hydroxylase (TH) in non-dividing neurons, which was associated with an increase in striatal dopamine concentrations and a rescue of forelimb akinesia and spontaneous rotations. Phenotypic analysis using multiplexed iterative immunofluorescence imaging further revealed that most of the TH-positive cells in the striatum co-expressed the

dopaminergic marker DAT and the pan-neuronal marker NEUN, with the majority of these triple-positive cells being classified as mature GABAergic neurons. Additional research is needed to fully elucidate the molecular mechanisms underlying the expression of the observed markers and understand how the formation of these cells contributes to the rescue of spontaneous motor behaviors. Nevertheless, our findings support a model where neuronal, but not astrocytic, downregulation of PTBP1 can mitigate symptoms in PD mice.

Introduction

Parkinson's disease (PD) is a complex and multifactorial disorder, characterized by the progressive and irreversible loss of dopaminergic neurons (DANs) in the substantia nigra pars compacta (SNc), which leads to the disruption of the nigrostriatal pathway and depletion of striatal dopamine (Bloem et al., 2021; Gitler et al., 2017; Moore et al., 2005). The cause of PD is unknown and only a handful of genetic and environmental risk factors have been identified (Brown et al., 2005; de Lau and Breteler, 2006; Elbaz et al., 2007; Kalia and Lang, 2015), making the development of a curative therapy challenging. In fact, current treatment strategies do not focus on slowing down or halting disease progression, but rather aim to control symptoms and maintain the patients' quality of life (Stoker and Barker, 2020).

Recently emerging *in vivo* transdifferentiation approaches, which leverage the plasticity of specific somatic cell types, hold great promise for developing therapies targeting a wide range of neurodegenerative diseases, including PD (Cohen and Melton, 2011; Torper and Götz, 2017). Astrocytes are of particular interest for such cell fate-switching approaches. First, they are non-neuronal cells and thus not affected by neurodegeneration (Yu et al., 2020). Second, they can acquire certain characteristics of neural stem cells, including multipotency, when activated (Niu et al., 2013; Buffo et al., 2008; Robel et al., 2011; Shimada et al., 2012; Sirko et al., 2013). Finally, they are highly proliferative upon brain injuries such as neurodegeneration (Yu et al., 2021). Several *in vivo* studies have reported successful reprogramming of astrocytes to neurons via overexpression of proneuronal lineage-specific transcription factors, such as NEUROD1 or SOX2 (Guo et al., 2014; Niu et al., 2015, 2013). Moreover, two recent studies have shown that repression of the RNA-binding protein polypyrimidine tract binding protein 1 (PTBP1), which mainly functions as a splicing regulator (Valcárcel and Gebauer, 1997), efficiently converts astrocytes into DANs in the SNc or striatum (Qian et al., 2020; Zhou et al., 2020). Consequently, this led to the restoration of the nigrostriatal pathway and striatal dopamine levels, as well as rescue of motor deficits in a chemically-induced mouse model of PD (Qian et al., 2020; Zhou et al., 2020). However, since the publication of these two studies

69 in 2020, stringent lineage-tracing strategies have revealed that neither quiescent nor reactive
70 astrocytes convert to DANs upon PTBP1 depletion in the SNc or striatum (Chen et al., 2022;
71 Hoang et al., 2023; Wang et al., 2021), fueling widespread debate about the origin of these *de*
72 *novo* generated cells and their ability to alleviate motor deficits in PD mice (Arenas, 2020;
73 Jiang et al., 2021; Qian et al., 2021).
74 In this study, we emplyed adenine base editors (ABEs), which enable gene editing
75 independent of DNA double strand break formation (Gaudelli et al., 2017) and thus without
76 the risk of inducing chromosomal rearrangements, translocations, or large deletions
77 (Adikusuma et al., 2018; Kosicki et al., 2018; Shin et al., 2017), to install a loss-of-function
78 splice mutation in the *Ptbp1* gene in astrocytes or neurons. Using a chemically-induced PD
79 mouse model, we show that downregulation of neuronal rather than astroglial PTBP1 in the
80 SNc and striatum improves forelimb akinesia and spontaneous rotations. Histological analysis
81 revealed that downregulation of neuronal PTBP1 induced expression of tyrosine hydroxylase
82 (TH), which is the rate-limiting enzyme in the biosynthesis of dopamine and other
83 catecholamines and thus a characteristic marker of DANs, in non-dividing neurons of the
84 striatum. Since lack or dysfunction of TH results in dopamine deficiency and parkinsonism,
85 induction of TH expression in striatal neurons may explain the observed rescue of PD
86 phenotypes in mice and provide therapeutic benefits for PD patients.
87
88 **Results**
89 **Adenine base editing effectively downregulates PTBP1 in cell lines**
90 Base editors (BEs) are CRISPR-Cas derived genome engineering tools that allow the precise
91 conversion of A-T to G-C (adenine BEs, ABEs) or C-G to T-A (cytidine BEs, CBEs) base pairs
92 in cell lines as well as post-mitotic cells (Gaudelli et al., 2017; Koblan et al., 2021; Komor et
93 al., 2016; Levy et al., 2020; Villiger et al., 2018). BEs can thus be applied to precisely disrupt
94 canonical splice sites and permanently eliminate gene function *in vivo* (Kluesner et al., 2021;
95 Musunuru et al., 2021; Rothgangl et al., 2021; Winter et al., 2019). To achieve effective and
96 permanent repression of PTBP1, we sought to utilize ABEs to mutate canonical splice sites.
97 To assess if adenine base editing can be used to effectively disrupt PTBP1 expression, we
98 designed seven sgRNAs targeting canonical *Ptbp1* splice donor or acceptor sites in murine
99 Hepa1-6 cells (hereafter referred to as Hepa; Figure 1 – figure supplement 1). Plasmids
100 expressing the sgRNAs were co-delivered with *Sp*Cas-, *Sp*G-, or *Sp*Cas-NG-ABE-expressing
101 plasmids into Hepa cells, and genomic DNA was isolated at 5 days post-transfection for
102 analysis by deep sequencing. In line with previous reports (Kluesner et al., 2021), base editing

activity was higher at splice donor sites, with the highest editing rates at the exon-intron junctions of exon 3 (92.9±1.0% for *Sp*G-ABE8e) and 7 (85.0±7.2% for *Sp*Cas-ABE8e; figure 1 – figure supplement 1). Next, we validated whether both sgRNAs resulted in a reduction of transcript and protein levels. Average editing rates of 77% (sgRNA-ex3) and 73% (sgRNA-ex7) on genomic DNA (Figure 1 – figure supplement 2) resulted in approximately 70% and 50% reduction of *Ptbp1* transcripts in Hepa cells (Figure 1 - figure supplement 2), leading to a substantial reduction in PTBP1 protein levels and a significant increase in the transcription of exons known to be repressed by PTBP1 (Han et al., 2014; Li et al., 2014) (Figure 1 - figure supplement 2).

To analyze whether PTBP1 can also be downregulated by adenine base editing in neuronal and astroglial cells, we repeated experiments with sgRNA-ex3 and the ABE8e-*Sp*G variant in the neuronal Neuro2a and astroglial C8-D1A cell lines (hereafter referred to as N2a and C8-D1A). Compared to Hepa cells (92.9±1.0%; figure 1 – figure supplement 2), editing rates were lower in both cell lines (N2a: 64±7.9%; C8-D1A: 62.7±15.1%; figure 1A). Nevertheless, we again detected a substantial reduction of *Ptbp1* mRNA and PTBP1 protein levels (Figure 1B and C). Notably, editing of the canonical splice donor at exon 3 generated alternative *Ptbp1* splice sites in all three cell lines (Figure 1 – figure supplement 3), which, however, did not result in functional PTBP1 protein (Figure 1C; figure 1 - figure supplement 2). Based on these results, we decided to use sgRNA-ex3 in combination with the *Sp*G-ABE8e variant for *in vivo* experiments.

Downregulation of PTBP1 in neurons of the SNc generates TH-expressing cells

To study the effect of PTBP1 downregulation on an injured nigrostriatal circuit in mice, we first induced a unilateral lesion in the medial forebrain bundle (mfb) using the toxic dopamine analogue 6-hydroxydopamine (6-OHDA; figure 2 – figure supplement 1) (da Conceição et al., 2010), similar to previous studies (Chen et al., 2022; Hoang et al., 2023; Qian et al., 2020; Zhou et al., 2020). 5 weeks after the introduction of a lesion, we quantified the loss of TH^+ DANs in the SNc and DA fibers in the striatum by histology (Figure 2 - figure supplement 1). As expected, 6-OHDA induced a severe unilateral lesion in the nigrostriatal pathway (Figure 2 – figure supplement 1), characterized by an average 99% reduction in the number of TH^+ DANs in the SNc ipsilateral to the injection site (intact hemisphere: 10547±2313 TH^+ cells; lesioned hemisphere: 114±83 TH^+ cells; figure 2 – figure supplement 1) and an average 92% decrease in fluorescence signal corresponding to striatal DA fibers (dorsal and ventral; figure 2 – figure supplement 1). In line with previous reports (Chen et al., 2022), we also observed a sharp

137 increase in activated astrocytes, as indicated by the upregulation of the intermediate filament
138 protein GFAP (glial fibrillary acidic protein; figure 2 – figure supplement 1). Finally, we
139 analyzed perturbations in spontaneous motor activities following the 6-OHDA lesion (Boix et
140 al., 2015; Glajch et al., 2012; Iancu et al., 2005) and found that ipsilateral rotations and
141 contralateral forelimb akinesia were significantly increased (Figure 2 – figure supplement 1).
142 In order to target PTBP1 in astrocytes or neurons of 6-OHDA-induced PD mice, we designed
143 adeno-associated virus (AAV) vectors expressing the *Sp*G-ABE8e variant under the control of
144 the astrocyte-specific short GFAP promoter (Lee et al., 2008) (hereafter referred to as AAV-
145 GFAP), or the neuron-specific human synapsin 1 promoter (hsyn) (Kügler et al., 2003)
146 (hereafter referred to as AAV-hsyn). Both vectors additionally express sgRNA-ex3 under the
147 human U6 promoter (Duvoisin et al., 2012). As a non-targeting control, we generated an AAV
148 vector that expresses *Sp*G-ABE8e from the ubiquitous Cbh promoter (Gray et al., 2011), but
149 does not contain sgRNA-ex3 (hereafter referred to as AAV-ctrl). Since ABE8e exceeds the
150 packaging capacity of a single AAV (~5 kb including ITRs) (Grieger and Samulski, 2005), we
151 used the intein-mediated protein trans-splicing system from *Nostoc punctiforme* (*Npu*) (Li et
152 al., 2008; Truong et al., 2015) to split the ABE for expression from two separate AAVs (Figure
153 2 – figure supplement 2). After confirming on-target editing in N2a and C8-D1A cells (Figure
154 2 – supplement 2), we packaged intein-split ABE8e expression vectors into AAV-PHP.eB
155 capsids and delivered particles to the SNc of C57BL/6J mice 5 weeks after the introduction of
156 the unilateral 6-OHDA lesion (Figure 2A). 12 weeks after AAV treatment at a dose of 2×10^8
157 vector genomes (vg) per animal, we assessed whether the injured nigrostriatal pathway was
158 reconstituted (Figure 2A).
159 When we first analyzed animals treated with AAV-ctrl, we observed an average 99%
160 reduction of TH^+ cells in the SNc of lesioned animals (intact hemisphere: 8678±2765 TH^+ cells;
161 lesioned hemisphere: 122±26 TH^+ cells; Figure 2B and C). When we next assessed animals
162 treated with AAV-hsyn to downregulate PTBP1 in neurons, we observed a restoration of
163 approximately 10% of TH^+ cells compared to the intact hemisphere (intact hemisphere:
164 7613±1386 TH^+ cells; lesioned hemisphere: 721±144 TH^+ cells; Figure 2B and D). In contrast,
165 when we analyzed animals treated with AAV-GFAP to downregulate PTBP1 in astrocytes, we
166 did not observe TH^+ cells above control levels (intact hemisphere: 9209±1199 TH^+ cells;
167 lesioned hemisphere: 158±78 TH^+ cells; figure 2C and D; figure 2 – figure supplement 3).
168 However, despite the presence of TH+ cells in the SNc of AAV-hsyn-treated animals, we did
169 not detect an increase in fluorescence signal corresponding to DA fibers in the striatum,
170 suggesting that TH^+ cells generated in the SNc upon neuronal PTBP1 downregulation did not

171 form striatal projections (Figure 2E and F). Further supporting this observation, we did not
172 detect differences in fluorescence intensity between groups when analyzing projections of
173 DANs in the mfb (Figure 2 – figure supplement 4). Notably, base editing at the *Ptbp1* splice
174 site (AAV-ctrl, 0.04±0.03%, AAV-GFAP, 14.7±3.9%; AAV-hsyn, 15.5±8.5%) as well as a
175 reduction of *Ptbp1* transcript (AAV-GFAP, 23.7±12.7%; AAV-hsyn, 24.8±18.7%) and PTBP1
176 protein levels (AAV-GFAP, 10.8±6.3%; AAV-hsyn, 13.8±10.1%) could be confirmed in SNc
177 tissues at experimental endpoints (Figure 2 – figure supplement 5).
178 Taken together, our results suggest that PTBP1 downregulation in neurons of the SNc
179 generates TH^+ cells; however, unlike endogenous DANs in the SNc, they do not project to the
180 dorsal striatum.
181
182 **Downregulation of PTBP1 in neurons of the striatum generates TH^+ cells and increases**
183 **striatal dopamine levels**
184 Since the observed TH^+ cells in the SNc did not generate projections to reconstruct the
185 nigrostriatal pathway, we next tested whether we could bypass the lack of striatal projections
186 by generating TH^+ cells directly in the striatum. We therefore delivered AAV-hsyn at a dose of
187 4×10^8 vg per animal into the striatum of C57BL/6J mice, which were pre-treated with 6-OHDA
188 to generate a unilateral lesion. The injection volume, and thus the delivered AAV dose, was
189 increased compared to the SNc to achieve comparable AAV biodistribution in the larger
190 striatum. Confirming the unilateral impairment of the nigrostriatal pathway, analysis of brain
191 sections at 12 weeks post-treatment revealed an average 99% reduction of TH^+ cells in the
192 lesioned SNc and no detectable DA projections to the striatum (Figure 3 – figure supplement
193 1). When we quantified TH^+ cells in brain sections of the striatum, we found 106±38 TH^+ cells
194 across 3 sections (estimated as 2646±952 cells in the entire striatum) in mice treated with AAV-
195 hsyn compared to no TH^+ cells in the lesioned hemisphere of animals treated with AAV-ctrl
196 (Figure 3A). Analysis of striatum tissues isolated from AAV-ctrl- and AAV-hsyn-treated PD
197 mice revealed base editing at the *Ptbp1* splice site (AAV-ctrl, 0.4±0.1%; AAV-hsyn,
198 23.0±6.6%; Figure 3 – figure supplement 2) and downregulation of *Ptbp1* transcript (AAV-
199 hsyn, 30.8±14.6%) and PTBP1 protein levels (AAV-hsyn, 22.1±6.4%; figure 3 – supplement
200 2).
201 Since we did not observe PTBP1 downregulation or TH^+ cells in animals treated with AAV-
202 ctrl (Figure 3A; figure 3 – figure supplement 2), we can rule out that TH expression is induced
203 by 1) tissue damage due to the injection procedure or 2) toxicity due to the administered AAV
204 dose or serotype. To additionally exclude that TH expression might be caused by off-target

205 editing effects, we experimentally determined off-target sites of sgRNA-ex3 using GUIDE-seq
206 in N2a cells (Tsai et al., 2014) and subsequently analyzed these sites in treated animals by deep
207 amplicon sequencing (Figure 3 – supplement 3). One off-target site was identified in the
208 myopalladin (*Mypn*) gene, which encodes for a muscle-specific protein and plays a critical role
209 in regulating the structure and growth of skeletal and cardiac muscle (Filomena et al., 2021,
210 2020), and another site was detected in the intronic region of the ankyrin-1 (*Ank1*) gene, which
211 encodes for an adaptor protein linking membrane proteins to the underlying cytoskeleton
212 (Cunha and Mohler, 2009). Importantly, base editing rates at both sites were substantially lower
213 (*Mypn*, 5.4±1.7%; *Ank1*, 5.8±1.9%; Figure 3 – figure supplement 3) than at the *Ptbp1* site in
214 AAV-hsyn-treated mice (23.0±6.6%; Figure 3 – figure supplement 2) and no reduction in
215 transcript levels of the respective genes was observed (Figure 3 – figure supplement 3). Thus,
216 the induction of TH expression upon adenine base editing with sgRNA-ex3 is likely a direct
217 consequence of PTBP1 downregulation.
218 Next, we assessed whether the ectopic expression of TH in the striatum led to an increase in
219 tissue dopamine levels. We manually dissected striata of lesioned and unlesioned hemispheres
220 and quantified tissue dopamine levels by high-pressure liquid chromatography (HPLC; figure
221 3 – figure supplement 4). Peak identities and neurotransmitter concentrations were analyzed
222 using corresponding standards of known concentrations. Importantly, base edited animals
223 showed an approximately 2.5-fold increase in the concentration of striatal dopamine (AAV-
224 hsyn: 4.4±2.6 nmol/g protein; AAV-ctrl: 1.7±0.7 nmol/g protein) and the dopamine metabolite
225 3,4-dihydroxyphenylacetic acid (DOPAC; AAV-hsyn: 8.2±3.9 nmol/g protein; AAV-ctrl:
226 3.1±1.8 nmol/g protein) in the lesioned hemisphere (figure 3 – figure supplement 4).
227 Taken together, our data suggest that downregulation of PTBP1 in striatal neurons of 6-
228 OHDA-lesioned hemispheres resulted in the expression of TH and an elevation of striatal
229 dopamine concentrations.
230
231 **Phenotypic characterization of TH$^+$ cells in the striatum**
232 To characterize the TH-expressing cells in the SNc and striatum of AAV-hsyn-treated mice in
233 more detail, we co-stained them for the pan-neuronal marker NEUN (hexaribonucleotide
234 binding protein-3). As expected, virtually all TH$^+$ cells in the intact SNc were co-stained for
235 NEUN (99.0±0.1%; figure 3B). Likewise, the majority of TH$^+$ cells in the lesioned SNc
236 (hsyn: 92.0±6.2%; figure 3B) and striatum of AAV-hsyn-treated animals (77.5±11.8%; figure
237 3C) were also labelled by NEUN, further corroborating a neuronal origin of these cells.
238 Moreover, we observed a significant reduction in the surface area and Feret's diameter between

239 TH/NEUN double-positive cells in the lesioned striatum compared to endogenous DANs in the
240 intact SNc, or TH/NEUN double-positive cell bodies in the lesioned SNc of AAV-hsyn-treated
241 mice (Figure 3D).

242 Differences in the frequency of NEUN-labeling, as well as surface area and diameter of TH^+
243 cells in the striatum might be attributed to 1) varying maturation states of these cells, potentially
244 influenced by the local microenvironment of the SNc vs striatum, and/or 2) TH-expressing cells
245 originating from distinct neuronal subpopulations. In line with previous work (Qian et al.,
246 2020), injection of AAV-hsyn into the visual cortex did not lead to TH expression in local
247 neurons (Figure 3 – figure supplement 5; n=174 Cas9/NEUN double-positive cells), suggesting
248 that the local microenvironment indeed plays a contributing role in inducing TH expression in
249 the targeted neurons. To next analyze the origin of TH-expressing cells in the striatum, we first
250 assessed whether these cells originated from dividing neural progenitors or mature, non-
251 dividing neurons. We therefore supplied bromodeoxyuridine (BrdU)-containing drinking water
252 to 6-OHDA-lesioned mice after AAV-hsyn treatment (Figure 3 – figure supplement 6). After
253 confirming successful BrdU labeling of proliferating cells in the dentate gyrus (DG; figure 3 –
254 figure supplement 6), we performed BrdU/NEUN/TH co-staining experiments with striatal
255 sections. Microscopic analysis of 163 TH/NEUN double-positive cells revealed no co-labeling
256 with BrdU (Figure 3 – figure supplement 6), indicating that TH^+ cells were not generated *de*
257 *novo* and rather originated from non-proliferating mature neurons.

258 Next, we performed multiplexed iterative immunofluorescence imaging (4i) (Cole et al.,
259 2022) on tissue sections to further characterize the identity, origin, and differentiation state of
260 these cells (Figure 4). After successful validation of antibody specificities (Figure 4 –
261 supplement 1), we performed four 4i rounds using markers for neural progenitors (SOX2/sex
262 determining region Y-box 2, NES/neuroepithelial stem cell protein, DCX/doublecortin), DANs
263 (TH, DAT), and mature neurons (NEUN, CTIP2/COUP-TF-interacting protein 2,
264 SST/somatostatin, PV/parvalbumin, CALB2/calbindin 2). The majority of TH^+ cells also
265 expressed the marker DAT (75.2±5.6%; figure 4A, B), further corroborating the DA identity of
266 these cells. Moreover, supporting the results of our BrdU-labeling experiments (Figure 3 –
267 figure supplement 6), only a small fraction of TH/DAT double-positive cells were labeled for
268 markers of neural progenitors (SOX2, 9.1±2.4%; NESTIN, 2.1±0.5%; DCX, 2.6±0.8%; figure
269 4A, B). Instead, most TH/DAT-labeled cells expressed the adult pan-neuronal marker NEUN
270 (86.2±3.7%; figure 4A, B). Of this TH/DAT/NEUN-positive population, 49.8±12.9% were
271 additionally labeled with CTIP2 (Figure 4A and 4B), a marker for GABAergic medium spiny
272 neurons (MSNs), and 46.4±10.4% expressed markers for various GABAergic interneurons

273 (PV, 3.2±1.9%; SST, 3.5±1.2%; CALB2, 39.7±11.0%; figure 4A and 4B), indicating that
274 expression of DA markers may be achieved in various subtypes of GABAergic neurons upon
275 PTBP1 downregulation.
276 In summary, our data show that TH-expressing cells were not generated from proliferating
277 neural stem cells, but rather originated from various populations of post-mitotic striatal neurons
278 that acquired DA characteristics upon PTBP1 downregulation.
279
280 **Neuronal PTBP1 repression alleviates drug-free motor dysfunction in PD mice**
281 Last, we evaluated whether neuronal and/or astroglial base editing of PTBP1 in the SNc and/or
282 striatum could restore motor functions in mice with a unilateral 6-OHDA lesion. We first
283 performed two common drug-free behavioral tests: the cylinder test to quantify the asymmetry
284 of spontaneous rotations and the stepping test to quantify contralateral forelimb akinesia (Boix
285 et al., 2015; Glajch et al., 2012; Iancu et al., 2005). We found that drug-free motor dysfunctions
286 were significantly alleviated in animals treated with AAV-hsyn, but not with AAV-GFAP, in
287 the SNc when using an AAV dose of 2×10^8 vg per animal (Figure 5 – figure supplement 1).
288 Likewise, PTBP1 targeting in striatal neurons restored the asymmetry of spontaneous behaviors
289 (Figure 5A and 5B). To assess the extent of motor improvements in response to the ABE
290 treatment, we additionally tested two drug-induced motor behaviors. However, we did not
291 detect recovery of contralateral rotations in treated animals after systemic administration of
292 amphetamine (Figure 5C; figure 5 – figure supplement 1), which leads to an enhanced
293 imbalance of extracellular dopamine concentrations between the denervated and intact striatum
294 (Freyberg et al., 2016; Karam et al., 2022). Likewise, after systemic administration of
295 apomorphine, which acts as a dopamine receptor agonist and stimulates hypersensitive
296 dopamine receptors in the lesioned hemisphere (Arroyo-García et al., 2018; da Conceição et
297 al., 2010; Iancu et al., 2005), we did not observe a recovery of ipsilateral rotations in any
298 treatment group (Figure 5D; figure 5 – figure supplement 1).
299 Taken together, downregulation of PTBP1 in SNc and striatal neurons improves
300 spontaneous, but not drug-induced, behaviors in 6-OHDA-lesioned mice.
301
302 **Discussion**
303 In this study, we applied adenine base editing to introduce *Ptbp1* loss-of-function mutations in
304 astrocytes and neurons in the 6-OHDA-induced PD mouse model. Delivery of dual AAV
305 vectors to the SNc resulted in the formation of TH-expressing cells and rescue of spontaneous
306 behaviors when a neuronal promoter was used to drive ABE expression. However, no DA

307 projections to the striatum were detected, supporting recent findings that suggest a functional
308 role of PTBP1 in promoting axon regeneration of adult sensory neurons (Alber et al., 2023).
309 Reconstitution of the nigrostriatal pathway, which connects the SNc with the dorsal striatum
310 (Kalia and Lang, 2015), is therefore unlikely the mechanism underlying the observed
311 phenotypic rescue. Supporting this hypothesis, downregulation of neuronal PTBP1 in the
312 striatum of 6-OHDA-lesioned mice also led to the formation of TH^+ cells and a rescue of
313 spontaneous behaviors.
314 Two previous studies suggested that PTBP1 downregulation in the SNc, using either
315 shRNA-mediated knockdown or knockdown via CRISPR-CasRx, led to the conversion of
316 astrocytes into functional DANs in 6-OHDA-lesioned mice (Qian et al., 2020; Zhou et al.,
317 2020). However, recent lineage tracing studies revealed that neither quiescent nor reactive
318 astrocytes in the SNc or striatum convert to DANs upon PTBP1 downregulation (Chen et al.,
319 2022; Hoang et al., 2023; Wang et al., 2021). Instead, these studies hypothesize that the reported
320 effects might be attributed to leaky activation of the GFAP promoter in neurons, which could
321 have been misinterpreted as astrocyte to neuron conversion. Our study contributes to this
322 recently growing body of evidence, indicating that downregulation of astroglial PTBP1 does
323 not induce astrocyte conversion into DANs, and that neurons are the origin of the observed TH^+
324 cells (Chen et al., 2022; Wang et al., 2021; Yang et al., 2023). Our 4i and BrdU experiments
325 furthermore revealed that TH expression in the striatum was induced in mature neurons, either
326 expressing markers of GABAergic MSNs or interneurons. These findings indicate that the
327 induction of TH expression is not restricted to a specific neuronal subpopulation, but may rather
328 be attributed to 1) potential bias of hsyn promoter activity towards inhibitory neurons
329 (Radhiyanti et al., 2021), 2) preferential AAV tropism towards distinct neuronal
330 subpopulations in the striatum, or 3) differences in the local microenvironment, chemical
331 signals, and neuronal circuitry required to induce TH expression in distinct neuronal
332 subpopulations.
333
334 While our study suggests that PTBP1 downregulation can enable TH expression in various
335 GABAergic neuronal populations in the striatum, the transcriptional changes leading to and
336 following TH expression in these cells remain unclear. Previous research has demonstrated that
337 the interplay between microRNAs (miRNAs) and the RNA processing proteins PTBP1 and its
338 homology nPTBP (PTBP2) is crucial during neuronal differentiation and maturation (Fig. 5 –
339 figure supplement 2) (Boutz et al., 2007; Makeyev et al., 2007; Zheng et al., 2012). Key events
340 in this signaling cascade are the dynamic release of PTBP1-mediated inhibition of miRNA-124,

341 which induces nPTBP expression and activates neuron-specific expression programs in non-
342 neuronal cells (Makeyev et al., 2007; Xue et al., 2013). Thus, the activation of the
343 PTBP1/nPTBP regulatory loops is essential for driving reprogramming towards the neuronal
344 lineage and subsequent neuronal maturation (Xue et al., 2016, 2013). While this classical model
345 of PTBP1 down-regulation and neuronal differentiation implies neglible expression or
346 importance of PTBP1 in mature neurons, our results indicate that PTBP1 is sufficiently
347 expressed and plays a functional role in mature neurons, with the installation of a loss-of-
348 function mutation resulting in detectable reduction in relative protein amounts (Figure 2 –
349 supplement 5; figure 3 – supplement 2) and behavioral improvements in a PD mouse model
350 (Figure 5; figure 5 – supplement 1). Supporting these findings, a recent study demonstrated
351 PTBP1 expression in axons of sensory and motor neurons as well as a functional role in
352 sensation, injury response, and axonal regeneration (Alber et al., 2023). Further investigation
353 using single cell transcriptional analysis of the PTBP1/nPTBP regulatory loops, pro-neuronal
354 transcription factors (*Ascl1*, *Myt1l*, *Zic1*, *Brn2*, *NeuroD1*) (Xue et al., 2013), or transcription
355 factors guiding the differentiation into DANs (*Nr4a2*, *LMx1a*, *LMx1b*, or *Pitx3* (Niu et al.,
356 2021)) could provide insights into the transcriptional switches underlying TH expression in
357 MSNs and interneurons as observed in our study.
358 MSNs, the principal neurons of the striatum (~95%), can be divided into two distinct
359 subtypes based on their expression of dopamine receptors and their axonal projections (D1- or
360 D2-MSNs) (Gerfen et al., 1990; Smith et al., 1998). Both the input to and output from D1- and
361 D2-MSNs are dynamically controlled by striatal interneurons, which constitute approximately
362 5% of total striatal neurons (Clarke and Adermark, 2015). Since both MSNs and interneurons
363 receive DA inputs from the SNc, their activity and excitability are strongly hampered when
364 striatal dopamine is absent (Bamford et al., 2018; Gerfen and Surmeier, 2011; Kreitzer and
365 Malenka, 2008). It therefore seems feasible that PTBP1 downregulation by adenine base editing
366 and subsequent TH expression might have enabled local dopamine synthesis in the dorsal
367 striatum, which may have been sufficient to partly restore the function of these cell populations
368 and compensate for the depletion of DA inputs from the SNc. Supporting this hypothesis, a
369 recent study has shown that depletion of the orphan G-protein coupled receptor 6 (GPR6) in
370 D2-MSNs reduced intracellular cyclic adenosine monophosphate (cAMP) concentrations,
371 leading to increased striatal dopamine and decreased involuntary movements following
372 apomorphine treatment in 6-OHDA-lesioned PD mice (Sun et al., 2021). When we quantified
373 dopamine levels in the striatum of AAV-hsyn-treated PD mice using HPLC, we observed a 2.5-
374 fold increase in striatal dopamine, suggesting that induction of TH expression in striatal neurons

375 might establish a basal tone of extracellular dopamine despite the absence of striatal DA
376 projections, akin to pharmacological replenishment in PD patients (Poewe et al., 2017). While
377 the increase in dopamine levels was modest compared to 6-OHDA-lesioned rats treated with
378 the dopamine precursor L-DOPA, which exhibited an increase in extracellular dopamine
379 concentrations from ~0.04 fmol/µL to ~9-10 fmol/µL (Lindgren et al., 2010), our results
380 indicate that even a modest increase in striatal dopamine is sufficient to rescue spontaneous
381 motor behaviors in PD mice. This finding aligns with recent work showing that multiple
382 unconditioned DA-dependent motor tasks can be sustained through a diffuse basal tone of
383 extracellular dopamine in the striatum (Delignat-Lavaud et al., 2023). Conversely, basal
384 dopamine levels were insufficient to improve amphetamine-induced behaviors in AAV-hsyn-
385 treated PD mice in this study, potentially due to the lack of striatal projections from the SNc
386 and/or insufficient availability of intracellular dopamine in striatal neurons. Likewise, the
387 detected dopamine levels in striatal tissues were not sufficient to reverse the hypersensitivity of
388 D1 and D2 receptors to the dopamine agonist apomorphine. Higher base editing rates,
389 achievable using either single AAV delivery of smaller Cas9 orthologues or multiple injections
390 into the rostral, medial, and caudal regions of the striatum, may result in more pronounced
391 global PTBP1 downregulation and potentially higher tissue dopamine concentrations, leading
392 to a broader behavioral rescue. Moreover, further analysis using fiber photometry or
393 microdialysis could provide information on synaptic dopamine release and availability.
394
395 Transcriptional reprogramming is fundamental for neuronal differentiation and maturation,
396 relying on various feedback and feed-forward circuits to regulate cell type-specific gene
397 expression programs. While loss of PTBP1 is considered crucial for reducing neuronal
398 apoptosis and inducing neuronal differentiation during development, its various roles in mature
399 neurons during adulthood remains largely elusive. Further investigation using single cell
400 transcriptional analysis or spatial transcriptomics is needed to identify the transcriptional
401 changes driving the expression of DA markers in striatal GABAergic neurons upon PTBP1
402 downregulation. These experiments may also contribute to our understanding of how PTBP1
403 downregulation may affect cAMP metabolism, dopamine synthesis, and basal ganglia circuitry
404 in PD mice. Finally, to fully explore the therapeutic potential of PTBP1 base editing, future
405 studies should also combine detailed transcriptional analysis with stringent lineage-tracing
406 technologies and *in vivo* assessment of synaptic dopamine availability and release in more
407 sophisticated PD mouse models that exhibit neuropathological, motor, and cognitive aspects of
408 the disease.

409 **Materials and methods**

410

411 Generation of plasmids

412 sgRNA plasmids were generated by ligating annealed and phosphorylated oligos into a BsmBI-
413 digested lentiGuide-Puro (Addgene #52963) using T4 DNA ligase (NEB). To generate intein-
414 split ABE plasmids for AAV production, inserts with homology overhangs were either ordered
415 as gBlocks (IDT) or generated by PCR. Inserts were cloned into KpnI- and AgeI-digested AAV
416 backbones using HiFi DNA Assembly Master Mix (NEB). All PCRs were performed using Q5
417 High-Fidelity DNA Polymerase (NEB). All plasmids were transformed into *Escherichia coli*
418 Stable3 competent cells (NEB). The identity of all plasmids was confirmed by Sanger
419 Sequencing. Primers used for cloning of all plasmids are listed in supplementary tables 1 and
420 2. LentiGuide-Puro was a gift from F. Zhang (Addgene plasmid nos. 52963).

421

422 Cell culture transfection and genomic DNA preparation

423 Hepa1-6 (ATCC CRL-1830) cells were maintained in Dulbecco's modified Eagle's medium
424 (DMEM) plus GlutaMAX (Thermo Fisher Scientific), supplemented with 10% (v/v) fetal
425 bovine serum (FBS) and 1% penicillin/streptomycin (Thermo Fisher Scientific) at 37°C and
426 5% CO_2. Neuro2a (ATCC CCL-131) cells were maintained in Eagle's Minimum Essential
427 Medium (EMEM), supplemented with 10% (v/v) FBS and 1% penicillin/streptomycin. C8-
428 D1A [astrocyte type I clone, ATCC CRL-2541] were maintained in Dulbecco's modified
429 Eagle's medium (DMEM) supplemented with 10% (v/v) fetal bovine serum (FBS) and 1%
430 penicillin/streptomycin (Thermo Fisher Scientific) at 37°C and 5% CO_2. Cells were passaged
431 every 3 to 4 days and maintained at confluency below 90%.

432 For the *in vitro* screening of sgRNA activities, cells were seeded in 96-well cell culture
433 plates (Greiner) and transfected at 70% confluency using 0.5µl Lipofectamine™ 2000 (Thermo
434 Fisher Scientific). If not stated otherwise, 300ng of BE and 100ng of sgRNA were used for
435 transfections. Cells were incubated for 5 days after transfection and genomic DNA was isolated
436 using a direct lysis as previously described (Böck et al., 2022). For analysis of transcript and
437 protein levels, cells were seeded in a 48-well cell culture plate (Greiner) and transfected at 70%
438 confluency using 1µl of Lipofectamine™ 2000 (Thermo Fisher Scientific). A small aliquot of
439 the cells was used for isolation of genomic DNA by direct lysis as previously described (Böck
440 et al., 2022). The remaining cells were split in half for RNA and protein isolation.

441 For the assessment of *in vivo* base editing performance, a 40 µm thick section of the SNc or
442 striatum was used for manual dissection of these regions under a stereomicroscope. DNA was

443 subsequently isolated from tissue pieces by direct lysis as previously described (Böck et al.,
444 2022).
445
446 RNA isolation and RT-qPCR
447 RNA was isolated from cultured cells or snap-frozen brain tissues (striatum or SNc) using the
448 RNeasy Mini Kit (Qiagen) or the AllPrep DNA/RNA/Protein Mini Kit (Qiagen) according to
449 the manufacturer's instructions. RNA (1000ng input) was subsequently reverse-transcribed to
450 cDNA using random primers and the GoScript reverse transcriptase kit (Promega). RT-qPCR
451 was performed using FIREPolymerase qPCR Master Mix (Solis BioDyne) and analyzed using
452 a Lightcycler 480 system (Roche). Fold changes were calculated using the double ΔCt method.
453 Primers used for RT-qPCR are listed in supplementary table 3.
454
455 Protein isolation and western blot
456 Protein was isolated from cultured cells or snap-frozen brain tissues (striatum or SNc) using
457 radioimmunoprecipitation (RIPA) assay buffer (150 mM Tris pH 8.0, 150 mM NaCl, 0.1%
458 SDS, 0.5% sodium deoxycholate, 1% NP-40; Thermo Fisher Scientific), supplemented with
459 protease inhibitor cocktail (Roche), or the AllPrep DNA/RNA/Protein Mini Kit (Qiagen)
460 according to the manufacturer's instructions. Protein concentrations of all samples were
461 determined using the Pierce Bicinchoninic Acid (BCA) Protein Assay Kit (Thermo Fisher
462 Scientific).
463 Equal amounts of protein (*in vitro* samples: 30 µg; *in vivo* samples: 40 µg) were separated
464 by SDS-polyacrylamide gel electrophoresis (Thermo Fisher Scientific) and transferred to a
465 0.45-µm nitrocellulose membrane (Amersham). Membranes were incubated with rabbit anti-
466 PTBP1 (1:10,000; cat. no. ab133734, Abcam) and mouse anti-actin beta (1:2,000; cat. no.
467 ab8226; Abcam). Signals were detected by fluorescence using IRDye-conjugated secondary
468 antibodies (LI-COR Biosciences) and a LICOR Odyssey ® DLx imaging system. Protein
469 quantifications were performed in Fiji. All antibodies are listed in supplementary table 4.
470
471 Amplification for deep sequencing
472 PTBP1-specific oligos were used to generate targeted amplicons for deep sequencing. Input
473 genomic DNA was first amplified in a 10µL reaction for 30 cycles using NEBNext High-
474 Fidelity 2×PCR Master Mix (NEB). Amplicons were purified using AMPure XP beads
475 (Beckman Coulter) and subsequently amplified for eight cycles using oligos with sequencing
476 adapters. Approximately equal amounts of PCR products were pooled, gel purified, and

477 quantified using a Qubit 3.0 fluorometer and the dsDNA HS Assay Kit (Thermo Fisher
478 Scientific). Paired-end sequencing of purified libraries was performed on an Illumina Miseq
479 platform. Oligos for deep sequencing are listed in supplementary table 5.
480
481 HTS data analysis
482 Sequencing reads were first demultiplexed using the Miseq Reporter (Illumina). Next,
483 amplicon sequences were aligned to their reference sequences using CRISPResso2 (Clement
484 et al., 2019). Adenine base editing efficiencies at splice sites were calculated as percentage of
485 (number of reads containing edits at splice site)/(number of total aligned reads). Reference
486 nucleotide sequences are listed in supplementary table 6.
487
488 GUIDE-seq off-target analysis
489 Briefly, 6×10^4 N2a cells were plated in a 24-well plate one day prior to transfection. Cells were
490 transfected using Lipofectamine 3000 according to the manufacturer's instructions. Three
491 plasmids, encoding for the *Sp*G Cas9 nuclease [333 ng], the *Ptbp1* sgRNA-3 [167 ng], and GFP
492 [6 ng], were co-transfected with 12 pmol of the double-stranded oligodeoxynucleotide
493 (dsODN) following the the original GUIDE-seq protocol (Tsai et al., 2014). Transfections were
494 performed in triplicates. dsODN was transfected as a negative control. Cells were harvested
495 ~96 h post-transfection and genomic DNA was purified. Efficient indel formation at the on-
496 target site and integration of the dsODN tag were confirmed through deep amplicon
497 sequencing. Genomic DNA was subsequently sheared with Covaris E220 to on average 500 bp
498 according to the manufacturer's protocol. Sample libraries were assembled as previously
499 described (Tsai et al., 2014) and sequenced using the Illumina MiSeq platform. Data were
500 analysed using open-source guideseq software (version 1.1) (Tsai et al., 2016). Consolidated
501 reads were mapped to the mouse mm39 reference genome. Upon identification of the genomic
502 regions integrating the dsODNs in the aligned data, off-target sites with maximum six
503 mismatches to the on-target site, which were absent in the background controls, were retained.
504 A summary of the GUIDE-seq results can be found in Supplementary File 1.
505
506 AAV production
507 Pseudo-typed vectors (AAV2 serotype PHP.eB) were produced by the Viral Vector Facility of
508 the Neuroscience Center Zurich. Briefly, AAV vectors were ultracentrifuged and diafiltered.
509 Physical titers (vector genomes per milliliter, vg/mL) were determined using a Qubit 3.0

510 fluorometer (Thermo Fisher Scientific) as previously published (Düring et al., 2020). The
511 identity of the packaged genomes of each AAV vector was confirmed by Sanger sequencing.
512
513 Animal studies
514 Animal experiments were performed in accordance with protocols approved by the Kantonales
515 Veterinäramt Zürich and in compliance with all relevant ethical regulations. C57BL/6J mice
516 were housed in a pathogen-free animal facility at the Institute of Pharmacology and Toxicology
517 of the University of Zurich. Mice were kept in a temperature- and humidity-controlled room
518 on a 12-hour light-dark cycle. Mice were fed a standard laboratory chow (Kliba Nafag no. 3437
519 with 18.5% crude protein) with ad libitum access to food and water. Exclusion criteria were
520 pre-defined during study design to meet ethical regulations. No animal was excluded from the
521 study.
522
523 Stereotactic injections in mice
524 Unless stated otherwise, adult female C57BL/6J mice at P50-P60 were used to introduce a
525 unilateral lesion in the medial forebrain bundle. Buprenorphine [0.1 mg/kg bodyweight], was
526 administered to mice subcutaneously 30 min prior to surgery. Animals were anesthetized using
527 isoflurane (5% isoflurane with 1000 mL/min in 100% O_2) and placed into a stereotaxic mouse
528 frame on a warming surface to maintain body temperature. Anesthesia was maintained at 1.5-
529 2.5% isoflurane with 400 mL/min in 100% O_2 during surgeries. Mice were pre-treated with
530 desipramine [25 mg/kg bodyweight] and pargyline [5 mg/kg bodyweight] 30 min before the
531 injection of 6-hydroxydopamine (6-OHDA) was performed. 6-OHDA was dissolved in 0.02%
532 ascorbate/saline solution at a concentration of 15 mg/mL and used within a maximum of 3h.
533 3.6μg of 6-OHDA were injected into the medial forebrain bundle (mfb) at the following
534 coordinates (relative to bregma): -1.2 mm anteroposterior (AP); 1.3 mm mediolateral (ML);
535 -5 mm dorsoventral (DV). Sham-injected mice were injected with 0.02% ascorbate/saline
536 solution. Injections were performed using a 5μL Hamilton syringe with a 33G needle at a speed
537 of 0.05 μL/min. The needle was slowly removed 3min after the injection and the wound was
538 sutured using Vicryl 5-0 suture (Ethicon). Animals with unilateral lesions received extensive
539 post-operative care for two weeks. After the lesion, animals received daily glucose injections,
540 and kitten milk (Royal Canin) for one week to support recovery.
541 4-5 weeks after the introduction of the 6-OHDA lesion, AAVs were injected into the
542 substantia nigra, striatum, or visual cortex at the following coordinates (relative to bregma):
543 -3.0 mm anteroposterior (A/P), 1.2 mm mediolateral (M/L), -4.5 mm dorsoventral (D/V) for

544 the substantia nigra pars compacta; 0.38 mm A/P, 1.8 mm M/L, -4:0.4:-2.4 mm D/V for the
545 striatum; and -4.5 mm A/P, 2.7 mm ML, 0.35 mm D/V for the visual cortex. Injections were
546 performed using the same size needle, syringe, and speed as before. The needle was slowly
547 removed 3min after the injection and the wound was sutured using Vicryl 5-0 suture (Ethicon).
548
549 Behavioral assays
550 Behavior experiments were performed at 4 weeks after the 6-OHDA lesion and 12 weeks after
551 delivery of the treatment. Scientists performing and analyzing behavioral data were blinded
552 during the study. To analyze spontaneous rotations during the dark phase of the light cycle,
553 mice were individually placed into a glass cylinder (10cm diameter, 14cm height) and after
554 1min of habituation mouse behavior was recorded from the bottom using a digital camera. For
555 assessment of spontaneous rotations after treatment, animals were first habituated to the
556 experimental environment on three separate days. Full body ipsi- and contralateral turns (360°)
557 were counted for 10min. A frame-by-frame video player (VLC media player) was used for
558 scoring. Data are expressed as a percentage of ipsilateral rotations from total rotations.
559 To assess forelimb akinesia during the light phase of the light cycle, we quantified left and
560 right forelimb usage in the stepping test (Blume et al., 2009; Olsson et al., 1995). First, the
561 animal was allowed to settle at one edge of the table (~2s) with all limbs on the table. Next, the
562 experimenter lifted the hind legs of the mouse by pulling up the tail, leaving only the forepaws
563 touching the table. Animals were pulled backwards by the tail at a steady pace of approximately
564 1m in 3-4s for a total distance of 1m. Two trials of three consecutive repetitions were performed
565 per animal with at least 10min break between the two trials. Behavior was recorded from the
566 side using a digital camera and the number of adjusting steps from both forepaws was counted.
567 Data are represented as percentage of ipsilateral steps from total steps.
568 For assessing drug-induced rotations, D-amphetamine (5 mg/kg bodyweight; Sigma-
569 Aldrich) or apomorphine (0.5 mg/kg bodyweight; Sigma-Aldrich) was administered to mice
570 via intraperitoneal injections. Following the injection, mice were placed in a recovery cage for
571 10min. Afterwards, mice were placed in a cylinder (10cm diameter, 15cm height) and
572 habituated for 1min. Rotations induced by D-amphetamine or apomorphine were recorded from
573 the bottom for 10min using a digital camera and only fully-body turns (360°) were counted as
574 previously described. Data are expressed as percentage of ipsilateral or contralateral rotations
575 from total rotations.
576
577 Trans-cardiac perfusion, brain isolation, and dissection of brain regions

578 Sodium pentobarbital (Kantonsapotheke Zürich) was injected via intraperitoneal injection at a
579 dose of 100mg/kg. Complete anesthesia was confirmed by the absence of a toe pinch reflex.
580 Mice were placed on a perfusion stage inside a collection pan and the peritoneal cavity was
581 exposed. The diaphragm was cut through laterally and the rib cage was cut parallel to the lungs,
582 creating a chest "flap". The flap was clamped in place using a hemostat (Fine Science Tools)
583 and a 25G needle (Sterican), attached to silicon tubing and a peristaltic pump, was inserted into
584 the left ventricle. The right atrium was cut for drainage. Animals were first perfused with ice-
585 cold PBS (Thermo Fisher Scientific) at a rate of 10mL/min, followed by perfusion with ice-
586 cold fixative at the same rate (4% paraformaldehyde, PFA, Sigma-Aldrich). Once the perfusion
587 was complete, mice were decapitated and the skull was removed with scissors and tweezers
588 without inflicting damage to the underlying tissue. The brain was removed using a spatula.
589 For histology, PFA-perfused brains were post-fixated in 4% PFA for 4h, followed by
590 overnight incubation in 30% sucrose. For neurotransmitter quantifications, brains were
591 isolated, rinsed in PBS, and cut into 1mm slices using an acrylic mouse brain matrix (AgnThos)
592 and razor blades. The striatum was isolated under a stereomicroscope using the mouse brain
593 atlas (Paxinos and Franklin, 2001). For amplicon sequencing, regions of interest (striatum or
594 SNc) were manually dissected from 40µm-thick coronal sections under a stereomicroscope
595 using the mouse brain atlas (Paxinos and Franklin, 2001).
596
597 Immunohistochemistry
598 Fresh or snap-frozen PFA-fixed brain tissues of C57BL/6J mice were cut into 40µm-thick
599 sections using a microtome. Sections were blocked in PBS supplemented with 5% normal
600 donkey serum (cat. no. ab7475, abcam) and 0.3% Triton X-100 (Sigma-Aldrich) for 1h. Brain
601 sections were incubated with primary antibodies overnight at 4°C (rabbit-NEUN, 1:1'000,
602 abcam 177487; mouse-TH; 1:1'000, Immunostar 22941; chicken-GFAP, 1:1'500, abcam
603 ab95231; rat-BrdU, 1:400, Oxford Biotech OBT0030). Donkey anti-rabbit-488 (1:1'000),
604 donkey anti-mouse-594 (1:500), donkey anti-chicken-647 (1:500) and donkey anti-rat-647
605 (1:500; all from Jackson ImmunoResearch) were used as secondary antibodies and sections
606 were counterstained with 4′,6-diamidino-2-phenylindole (DAPI, Sigma-Aldrich). Mounting
607 was performed using Prolong Gold Antifade Mountant (Thermo Fisher Scientific). Images
608 were taken with a Zeiss LSM 900 or a Zeiss AxioScan.Z1 slidescanner and analyzed with Fiji
609 (Schindelin et al., 2012) or cell profiler (Stirling et al., 2021). The numerical density of cells
610 was estimated using optical dissection (NvVref method). Density of striatal fibres in the
611 lesioned hemisphere was quantified as relative fluorescence intensity (FI) compared to the

612 intact hemisphere. Additionally, the FI of the TH staining detected in the corpus callosum of
613 each hemisphere was used for background correction of the FI detected in the striatum of the
614 same hemisphere. Antibodies are listed in supplementary table 4.
615
616 Iterative immunofluorescence imaging (4i) and image analysis
617 Frozen PFA-fixed brain tissues of C57BL/6J mice were cut into 40µm-thick sections using a
618 microtome. Before mounting the sections, glass-bottomed 24-well plates (Cellvis P24-1.5H-
619 N) were coated with poly-D-lysine (0.1mg/mL, Sigma-Aldrich) for 5min at RT on a shaker.
620 Afterwards, wells were rinsed three times with deionized water and left to dry overnight. Tissue
621 sections were washed three times in PBS and transferred into the coated wells containing
622 500µL of PBS, which was carefully aspirated with a glass pipette to allow the sections to adhere
623 flat to the bottom. Sections were left to dry until there was no visible liquid remaining around
624 the edges of the sections. Next, tissue sections were rinsed with PBS (3×5min), followed by 1h
625 incubation in blocking solution (PBS supplemented with 3% donkey serum, 0.5% Triton X-
626 100, and 0.025% PFA) at RT. Sections were then incubated in primary antibodies (list in
627 supplementary table 4), diluted in blocking solution, for 3 nights at 4°C. Next, sections were
628 washed in PBS (3×5min), rinsed in blocking solution for 5min, followed by incubation with
629 secondary antibodies and DAPI (1:1000; stock 1mg/mL) for 2h at RT. All following steps were
630 performed under low light conditions to reduce possible fluorophore crosslinking. Last,
631 sections were washed in PBS (3×5min) and imaging buffer (PBS supplemented with N-Acetyl-
632 cysteine at 0.7M final concentration, pH 7.4) was added at least 5min prior to imaging to
633 guarantee penetrance of tissue sections. Once the imaging cycle had finished, sections were
634 rinsed three times with dH_20 and incubated in equal amounts of dH_20 and elution buffer
635 (3×5min; 0.5M L-glycine, 3M urea, 3M guanidine hydrochloride, 0.07M TCEP-HCl; pH 2.5).
636 Successful elution of each antibody was visually confirmed using a fluoresence microscope.
637 After elution, tissue sections were washed three times in PBS (5min) and then another 4i round
638 was started. A total of 4 imaging cycles were performed.
639 All 4i z-stacks (image intervals of 0.5µm) were collected on an ImageXpress Confocal HT
640 confocal laser-scanning microscope with a 20x water objective (NA 0.95) using bi-directional
641 scanning. Samples of the same imaging cycle were labeled with the same antibodies and images
642 were collected with identical microscopy settings for laser power, gain, digital offset, pinhole
643 diameter, and z-step. Images from tile scans were exported using MetaXpress and analyzed
644 using Fiji (Schindelin et al., 2012). DAPI intensity patterns were used to align image tiles from
645 different staining cycles.

646

647 *In vivo* BrdU proliferation assay

648 Five days after delivery of the treatment, bromodeoxyuridine was administered to mice at a
649 concentration of 0.8 mg/mL via drinking water. Frozen PFA-fixed brain tissues of BrdU-
650 treated mice were cut into 40µm-thick sections using a microtome. Sections were washed
651 2×15min and 1×5min in PBS, followed by a 10min incubation in 1M HCl on ice, and a 25min
652 incubation in 2M HCl at 37°C. Next, tissues were rinsed in 0.1M borate buffer (Sigma-Aldrich)
653 for 10min on a shaker at RT. After the tissues were rinsed in PBS for 6×10min, brain tissues
654 were stained as described in section "Immunohistochemistry".

655

656 Neurotransmitter purification and UHPLC-ECD quantifications

657 Snap-frozen fresh striata of lesioned or unlesioned hemispheres were used for the purification
658 of neurotransmitters. All materials were kept cold on dry ice during the whole purification
659 procedure and samples were kept under low light conditions on ice. Tissue samples were
660 powderized with 2 pulses (at maximum intensity) using a CryoPrepTM system (Covaris).
661 Equal amounts of powder were transferred to a pre-cooled 2 mL tube. For homogenization of
662 the tissue powder, a metal ball (Qiagen) and 1mL homogenization buffer (100mM Tris-HCl,
663 2mM EDTA, pH 7.6 supplemented with protease inhibitor tablet) were added to each tube and
664 samples were homogenized for 2×90s at 20 Hz using a TissueLyser II (Qiagen). Next, samples
665 were centrifuged for 20min at maximum speed and 4°C. Lysates were next transferred to fresh
666 pre-cooled tubes and 1M HCl was added to a final concentration of 10% (v/v). Subsequently,
667 lysates were filtered using an Amicon Ultra 0.5 (Sigma-Aldrich) and a table top centrifuge
668 (30min at 4°C and maximum speed). 20µL of the filtered sample was used for quantification
669 of total protein amounts. Protein concentrations were determined using the ABBOT Alinity C
670 System (Abbot, Abbotpark, Illinois, USA, kit-no. 7P5920). 20µL of the filtered sample was
671 used in parallel for quantification of neurotransmitter levels by UHPLC-ECD. Brain
672 monoamine neurotransmitter metabolites were analyzed in the filtered lysate using a modified
673 Thermo Fisher UltiMate 3000 High Sensitivity HPLC Electrochemical System (Thermo Fisher
674 Scientific, Waltham, Massachusetts, USA). Injection volume of each sample was 20 µL and
675 separation of the compounds was achieved using an YMC-Hydrosphere UHPLC column (C18
676 12 nm, S-2.0 µm, 150 x 30 mm, YMC Inc., Wilmington, NC, USA). As a mobile phase, a
677 56.7mM sodium phosphate buffer, containing 5mM octanesulphonic acid, 50µM EDTA,
678 0.28% phosphoric acid (85%), and 23% methanol (pH 2.9-3.1, adjust with concentrated 10M
679 NaOH), was used with an isocratic flow rate of 410 µL/min. The column was maintained at

680 27°C by a surrounding TCC-3000SD column-thermostat. The analytical cell (Coulometric Cell
681 Model 6011RS, Thermo Fisher Scientific) within the electrochemical detector ECD-3000RS
682 (Thermo Fisher Scientific) was adjusted to a 10mV potential and 100µA gain range for the
683 upstream electrode, plus 400mV potential, plus 500nA gain range for the downstream electrode
684 with a response time of 1s. Data was analyzed using the Chromeleon Chromatography Data
685 System (CDS) Software 7.1.9 (Thermo Fisher) and corrected for the protein concentrations of
686 the respective homogenates. All measurements were performed at the clinical chemistry unit
687 of the Kinderspital Zürich.
688
689 Statistical analysis
690 All statistical analyses were performed using GraphPad Prism 10.2.0 for macOS. If not stated
691 otherwise, data are represented as biological replicates and are depicted as means±standard
692 deviation (s.d.). The sample size was approximated based on so-called Fermi methods and
693 experience from previous base editing studies during experimental design. Sample sizes and
694 the statistical analyses performed are described in the respective figure legends. Data were
695 tested for normality using the Shapiro-Wilk test if not stated otherwise. For all analyses, a *P*-
696 value of $P<0.05$ was considered statistically significant.
697
698 **Acknowledgements**
699 We thank the Functional Genomics Center Zurich (FGCZ) for technical support and access to
700 instruments at the University of Zurich. We thank Cornelia Schwerdel for technical support
701 during *in vitro* and staining experiments. Annina Denoth Lipuner and Sebastian Jessberger are
702 acknowledged for help with planning and setting up 4i experiments and sharing antibodies.
703 Members of the Schwank, Patriarchi, and Häberle labs are acknowledged for discussions and
704 comments on the manuscript.
705
706 **Funding information**
707 This work was supported by the Swiss National Science Foundation (SNSF) grant no.
708 310030_185293 (to G.S.) and 310030_196455 (to T.P.), Novartis Foundation for Medical-
709 Biological Research no. FN20-0000000203 (to D.B.), SNSF Spark fellowship no. 196287 (to
710 D.B.), the URPP Itinerare (to G.S. and to D.B.), the Helmut Horten Foundation (to G.S.), and
711 the European Research Council (ERC) under the European Union's Horizon 2020 research and
712 innovation program (grant agreement: 891959; to T.P.).
713

714 **Author contributions**

715 Conceptualization: D.B. and M.W.; Methodology: D.B. and M.W.; Investigation and
716 Validation: D.B., M.W., J.M., D.F.C., P.I.K., S.A.; Visualization: D.B. and P.I.K.; Formal
717 analysis: D.B., M.W., J.M., D.F.C., P.I.K., S.A., A.C., A.R., J.H., T.P., and G.S.; Resources
718 and Data curation: T.P. and G.S.; Writing – original draft: D.B.; Writing – review&editing:
719 D.B., M.W., J.M., D.F.C, P.I.K., S.A., A.C., A.R., J.H., T.P., and G.S.; Supervision and project
720 administration: D.B. and M.W.; Funding acquisition: D.B., T.P., and G.S..

721

722 **Data availability**

723 All data associated with this study are present in the paper. Illumina sequencing data is
724 available under accession number GSE237570 at the Gene Expression Omnibus (GEO) and
725 bioproject number PRJNA1155634 at the NCBI Sequence Read Archive.

726

727 **Competing interest declaration**

728 G.S. is an advisor to Prime Medicine.

729

730 **Correspondence**

731 Correspondence should be addressed to Tommaso Patriarchi (patriarchi@pharma.uzh.ch),
732 Gerald Schwank (schwank@pharma.uzh.ch), or Desiree Böck (desiree.boeck@uzh.ch).

733

734 **References**

735 Adikusuma F, Piltz S, Corbett MA, Turvey M, McColl SR, Helbig KJ, Beard MR, Hughes J,
736 Pomerantz RT, Thomas PQ. 2018. Large deletions induced by Cas9 cleavage. *Nature*.
737 doi:10.1038/s41586-018-0380-z

738 Alber S, Di Matteo P, Zdradzinski MD, Costa ID, Medzihradszky KF, Kawaguchi R, Di
739 Pizio A, Freund P, Panayotis N, Marvaldi L, Doron-Mandel E, Okladnikov N, Rishal I,
740 Nevo R, Coppola G, Joon Lee S, Sahoo PK, Burlingame AL, Twiss JL, Fainzilber M.
741 2023. PTBP1 regulates injury responses and sensory pathways in adult peripheral
742 neurons. *Sci Adv* **9**.
743 doi:10.1126/SCIADV.ADI0286/SUPPL_FILE/SCIADV.ADI0286_DATA_S1_AND_S
744 2.ZIP

745 Arenas E. 2020. Method to combat Parkinson's disease by astrocyte-to-neuron conversion.
746 *Nat 2021 5827813* **582**:489–490. doi:10.1038/d41586-020-01817-4

747 Arroyo-García LE, Vázquez-Roque RA, Díaz A, Treviño S, De La Cruz F, Flores G,

748 Rodríguez-Moreno A. 2018. The Effects of Non-selective Dopamine Receptor
749 Activation by Apomorphine in the Mouse Hippocampus. *Mol Neurobiol* **55**.
750 doi:10.1007/s12035-018-0991-2
751 Bamford NS, Wightman RM, Sulzer D. 2018. Dopamine's Effects on Corticostriatal
752 Synapses during Reward-Based Behaviors. *Neuron* **97**:494–510.
753 doi:10.1016/J.NEURON.2018.01.006
754 Bloem BR, Okun MS, Klein C. 2021. Parkinson's disease. *Lancet* **397**:2284–2303.
755 doi:10.1016/S0140-6736(21)00218-X
756 Blume SR, Cass DK, Tseng KY. 2009. Stepping test in mice: A reliable approach in
757 determining forelimb akinesia in MPTP-induced Parkinsonism. *Exp Neurol* **219**.
758 doi:10.1016/j.expneurol.2009.05.017
759 Böck D, Rothgangl T, Villiger L, Schmidheini L, Matsushita M, Mathis N, Ioannidi E,
760 Rimann N, Grisch-Chan HM, Kreutzer S, Kontarakis Z, Kopf M, Thöny B, Schwank G.
761 2022. In vivo prime editing of a metabolic liver disease in mice. *Sci Transl Med* **14**.
762 doi:10.1126/scitranslmed.abl9238
763 Boix J, Padel T, Paul G. 2015. A partial lesion model of Parkinson's disease in mice -
764 Characterization of a 6-OHDA-induced medial forebrain bundle lesion. *Behav Brain Res*
765 **284**. doi:10.1016/j.bbr.2015.01.053
766 Boutz PL, Stoilov P, Li Q, Lin CH, Chawla G, Ostrow K, Shiue L, Ares M, Black DL. 2007.
767 A post-transcriptional regulatory switch in polypyrimidine tract-binding proteins
768 reprograms alternative splicing in developing neurons. *Genes Dev* **21**:1636–1652.
769 doi:10.1101/GAD.1558107
770 Brown RC, Lockwood AH, Sonawane BR. 2005. Neurodegenerative diseases: An overview
771 of environmental risk factors. *Environ Health Perspect*. doi:10.1289/ehp.7567
772 Buffo A, Rite I, Tripathi P, Lepier A, Colak D, Horn AP, Mori T, Götz M. 2008. Origin and
773 progeny of reactive gliosis: A source of multipotent cells in the injured brain. *Proc Natl*
774 *Acad Sci U S A* **105**. doi:10.1073/pnas.0709002105
775 Chen W, Zhen Q, Huang Q, Ma S, Li M. 2022. Repressing PTBP1 fails to convert reactive
776 astrocytes to dopaminergic neurons in a 6-hydroxydopamine mouse model of
777 Parkinson's disease. *Elife* **11**. doi:10.7554/ELIFE.75636
778 Clement K, Rees H, Canver MC, Gehrke JM, Farouni R, Hsu JY, Cole MA, Liu DR, Joung
779 JK, Bauer DE, Pinello L. 2019. CRISPResso2 provides accurate and rapid genome
780 editing sequence analysis. *Nat Biotechnol*. doi:10.1038/s41587-019-0032-3
781 Cohen DE, Melton D. 2011. Turning straw into gold: Directing cell fate for regenerative

782 medicine. *Nat Rev Genet*. doi:10.1038/nrg2938
783 Cole JD, Del Castillo JS, Gut G, Gonzalez-Bohorquez D, Pelkmans L, Jessberger S. 2022.
784 Characterization of the neurogenic niche in the aging dentate gyrus using iterative
785 immunofluorescence imaging. *Elife* **11**. doi:10.7554/ELIFE.68000
786 Cunha SR, Mohler PJ. 2009. Ankyrin protein networks in membrane formation and
787 stabilization. *J Cell Mol Med* **13**:4364. doi:10.1111/J.1582-4934.2009.00943.X
788 da Conceição FSL, Ngo-Abdalla S, Houzel JC, Rehen SK. 2010. Murine model for
789 Parkinson's disease: From 6-OH dopamine lesion to behavioral test. *J Vis Exp*.
790 doi:10.3791/1376
791 de Lau LM, Breteler MM. 2006. Epidemiology of Parkinson's disease. *Lancet Neurol*.
792 doi:10.1016/S1474-4422(06)70471-9
793 Delignat-Lavaud B, Kano J, Ducrot C, Massé I, Mukherjee S, Giguère N, Moquin L,
794 Lévesque C, Burke S, Denis R, Bourque MJ, Tchung A, Rosa-Neto P, Lévesque D, De
795 Beaumont L, Trudeau LÉ. 2023. Synaptotagmin-1-dependent phasic axonal dopamine
796 release is dispensable for basic motor behaviors in mice. *Nat Commun 2023 141* **14**:1–
797 24. doi:10.1038/s41467-023-39805-7
798 Düring DN, Dittrich F, Rocha MD, Tachibana RO, Mori C, Okanoya K, Boehringer R, Ehret
799 B, Grewe BF, Gerber S, Ma S, Rauch M, Paterna JC, Kasper R, Gahr M, Hahnloser
800 RHR. 2020. Fast Retrograde Access to Projection Neuron Circuits Underlying Vocal
801 Learning in Songbirds. *Cell Rep* **33**. doi:10.1016/j.celrep.2020.108364
802 Duvoisin R, Ayuk MA, Rinaldi G, Suttiprapa S, Mann VH, Lee CM, Harris N, Brindley PJ.
803 2012. Human U6 promoter drives stronger shRNA activity than its schistosome
804 orthologue in Schistosoma mansoni and human fibrosarcoma cells. *Transgenic Res* **21**.
805 doi:10.1007/s11248-011-9548-0
806 Elbaz A, Dufouil C, Alpérovitch A. 2007. Interaction between genes and environment in
807 neurodegenerative diseases. *Comptes Rendus - Biol*. doi:10.1016/j.crvi.2007.02.018
808 Filomena MC, Yamamoto DL, Caremani M, Kadarla VK, Mastrototaro G, Serio S,
809 Vydyanath A, Mutarelli M, Garofalo A, Pertici I, Knöll R, Nigro V, Luther PK, Lieber
810 RL, Beck MR, Linari M, Bang ML. 2020. Myopalladin promotes muscle growth
811 through modulation of the serum response factor pathway. *J Cachexia Sarcopenia*
812 *Muscle* **11**:169. doi:10.1002/JCSM.12486
813 Filomena MC, Yamamoto DL, Carullo P, Medvedev R, Ghisleni A, Piroddi N, Scellini B,
814 Crispino R, D'autilia F, Zhang J, Felicetta A, Nemska S, Serio S, Tesi C, Catalucci D,
815 Linke WA, Polishchuk R, Poggesi C, Gautel M, Bang ML. 2021. Myopalladin knockout

816 mice develop cardiac dilation and show a maladaptive response to mechanical pressure
817 overload. *Elife* **10**. doi:10.7554/ELIFE.58313
818 Freyberg Z, Sonders MS, Aguilar JI, Hiranita T, Karam CS, Flores J, Pizzo AB, Zhang Y,
819 Farino ZJ, Chen A, Martin CA, Kopajtic TA, Fei H, Hu G, Lin YY, Mosharov E V.,
820 McCabe BD, Freyberg R, Wimalasena K, Hsin LW, Sames D, Krantz DE, Katz JL,
821 Sulzer D, Javitch JA. 2016. Mechanisms of amphetamine action illuminated through
822 optical monitoring of dopamine synaptic vesicles in Drosophila brain. *Nat Commun* **7**.
823 doi:10.1038/ncomms10652
824 Gaudelli NM, Komor AC, Rees HA, Packer MS, Badran AH, Bryson DI, Liu DR. 2017.
825 Programmable base editing of T to G C in genomic DNA without DNA cleavage.
826 *Nature*. doi:10.1038/nature24644
827 Gerfen CR, Surmeier DJ. 2011. Modulation of striatal projection systems by dopamine. *Annu*
828 *Rev Neurosci* **34**:441–466. doi:10.1146/ANNUREV-NEURO-061010-113641
829 Gitler AD, Dhillon P, Shorter J. 2017. Neurodegenerative disease: Models, mechanisms, and
830 a new hope. *DMM Dis Model Mech*. doi:10.1242/dmm.030205
831 Glajch KE, Fleming SM, Surmeier DJ, Osten P. 2012. Sensorimotor assessment of the
832 unilateral 6-hydroxydopamine mouse model of Parkinson's disease. *Behav Brain Res*
833 **230**. doi:10.1016/j.bbr.2011.12.007
834 Gray SJ, Foti SB, Schwartz JW, Bachaboina L, Taylor-Blake B, Coleman J, Ehlers MD,
835 Zylka MJ, McCown TJ, Samulski RJ. 2011. Optimizing promoters for recombinant
836 adeno-associated virus-mediated gene expression in the peripheral and central nervous
837 system using self-complementary vectors. *Hum Gene Ther* **22**.
838 doi:10.1089/hum.2010.245
839 Grieger JC, Samulski RJ. 2005. Packaging Capacity of Adeno-Associated Virus Serotypes:
840 Impact of Larger Genomes on Infectivity and Postentry Steps. *J Virol*.
841 doi:10.1128/jvi.79.15.9933-9944.2005
842 Guo Z, Zhang L, Wu Z, Chen Y, Wang F, Chen G. 2014. In vivo direct reprogramming of
843 reactive glial cells into functional neurons after brain injury and in an Alzheimer's
844 disease model. *Cell Stem Cell* **14**. doi:10.1016/j.stem.2013.12.001
845 Han A, Stoilov P, Linares AJ, Zhou Y, Fu XD, Black DL. 2014. De Novo Prediction of
846 PTBP1 Binding and Splicing Targets Reveals Unexpected Features of Its RNA
847 Recognition and Function. *PLoS Comput Biol* **10**. doi:10.1371/journal.pcbi.1003442
848 Hoang T, Kim DW, Appel H, Ozawa M, Zheng S, Kim J, Blackshaw S. 2023. Ptbp1 deletion
849 does not induce astrocyte-to-neuron conversion. *Nat 2023 6187964* **618**:E1–E7.

850 doi:10.1038/s41586-023-06066-9
851 Iancu R, Mohapel P, Brundin P, Paul G. 2005. Behavioral characterization of a unilateral 6-
852 OHDA-lesion model of Parkinson's disease in mice. *Behav Brain Res* **162**.
853 doi:10.1016/j.bbr.2005.02.023
854 Jiang Y, Wang Y, Huang Z. 2021. Targeting PTB as a One-Step Procedure for In Situ
855 Astrocyte-to-Dopamine Neuron Reprogramming in Parkinson's Disease. *Neurosci Bull*
856 **37**:430. doi:10.1007/S12264-021-00630-X
857 Kalia L V., Lang AE. 2015. Parkinson's disease. *Lancet*. doi:10.1016/S0140-6736(14)61393-
858 3
859 Karam CS, Williams BL, Jones SK, Javitch JA. 2022. The Role of the Dopamine Transporter
860 in the Effects of Amphetamine on Sleep and Sleep Architecture in Drosophila.
861 *Neurochem Res* **47**. doi:10.1007/s11064-021-03275-4
862 Kluesner MG, Lahr WS, Lonetree C lin, Smeester BA, Qiu X, Slipek NJ, Claudio Vázquez
863 PN, Pitzen SP, Pomeroy EJ, Vignes MJ, Lee SC, Bingea SP, Andrew AA, Webber BR,
864 Moriarity BS. 2021. CRISPR-Cas9 cytidine and adenosine base editing of splice-sites
865 mediates highly-efficient disruption of proteins in primary and immortalized cells. *Nat*
866 *Commun* **12**. doi:10.1038/s41467-021-22009-2
867 Kluesner MG, Nedveck DA, Lahr WS, Garbe JR, Abrahante JE, Webber BR, Moriarity BS.
868 2018. EditR: A Method to Quantify Base Editing from Sanger Sequencing. *Cris J*
869 **1**:239–250. doi:10.1089/CRISPR.2018.0014
870 Koblan LW, Erdos MR, Wilson C, Cabral WA, Levy JM, Xiong Z-M, Tavarez UL, Davison
871 LM, Gete YG, Mao X, Newby GA, Doherty SP, Narisu N, Sheng Q, Krilow C, Lin CY,
872 Gordon LB, Cao K, Collins FS, Brown JD, Liu DR. 2021. In vivo base editing rescues
873 Hutchinson–Gilford progeria syndrome in mice. *Nature*.
874 Komor AC, Kim YB, Packer MS, Zuris JA, Liu DR. 2016. Programmable editing of a target
875 base in genomic DNA without double-stranded DNA cleavage. *Nature*.
876 doi:10.1038/nature17946
877 Kosicki M, Tomberg K, Bradley A. 2018. Repair of double-strand breaks induced by
878 CRISPR–Cas9 leads to large deletions and complex rearrangements. *Nat Biotechnol*.
879 doi:10.1038/nbt.4192
880 Kreitzer AC, Malenka RC. 2008. Striatal Plasticity and Basal Ganglia Circuit Function.
881 *Neuron* **60**:543–554. doi:10.1016/J.NEURON.2008.11.005
882 Kügler S, Kilic E, Bähr M. 2003. Human synapsin 1 gene promoter confers highly neuron-
883 specific long-term transgene expression from an adenoviral vector in the adult rat brain

884 depending on the transduced area. *Gene Ther*. doi:10.1038/sj.gt.3301905
885 Lee Y, Messing A, Su M, Brenner M. 2008. GFAP promoter elements required for region-
886 specific and astrocyte-specific expression. *Glia* **56**. doi:10.1002/glia.20622
887 Levy JM, Yeh WH, Pendse N, Davis JR, Hennessey E, Butcher R, Koblan LW, Comander J,
888 Liu Q, Liu DR. 2020. Cytosine and adenine base editing of the brain, liver, retina, heart
889 and skeletal muscle of mice via adeno-associated viruses. *Nat Biomed Eng*.
890 doi:10.1038/s41551-019-0501-5
891 Li J, Sun W, Wang B, Xiao X, Liu XQ. 2008. Protein trans-splicing as a means for viral
892 vector-mediated in vivo gene therapy. *Hum Gene Ther*. doi:10.1089/hum.2008.009
893 Li Q, Zheng S, Han A, Lin C-H, Stoilov P, Fu X-D, Black DL. 2014. The splicing regulator
894 PTBP2 controls a program of embryonic splicing required for neuronal maturation. *Elife*
895 **3**. doi:10.7554/elife.01201
896 Lindgren HS, Andersson DR, Lagerkvist S, Nissbrandt H, Cenci MA. 2010. L-DOPA-
897 induced dopamine efflux in the striatum and the substantia nigra in a rat model of
898 Parkinson's disease: Temporal and quantitative relationship to the expression of
899 dyskinesia. *J Neurochem* **112**:1465–1476. doi:10.1111/J.1471-4159.2009.06556.X
900 Makeyev E V., Zhang J, Carrasco MA, Maniatis T. 2007. The MicroRNA miR-124 Promotes
901 Neuronal Differentiation by Triggering Brain-Specific Alternative Pre-mRNA Splicing.
902 *Mol Cell* **27**:435. doi:10.1016/J.MOLCEL.2007.07.015
903 Moore DJ, West AB, Dawson VL, Dawson TM. 2005. MOLECULAR
904 PATHOPHYSIOLOGY OF PARKINSON'S DISEASE. *Annu Rev Neurosci*.
905 doi:10.1146/annurev.neuro.28.061604.135718
906 Musunuru K, Chadwick AC, Mizoguchi T, Garcia SP, DeNizio JE, Reiss CW, Wang K, Iyer
907 S, Dutta C, Clendaniel V, Amaonye M, Beach A, Berth K, Biswas S, Braun MC, Chen
908 HM, Colace T V., Ganey JD, Gangopadhyay SA, Garrity R, Kasiewicz LN, Lavoie J,
909 Madsen JA, Matsumoto Y, Mazzola AM, Nasrullah YS, Nneji J, Ren H, Sanjeev A,
910 Shay M, Stahley MR, Fan SHY, Tam YK, Gaudelli NM, Ciaramella G, Stolz LE,
911 Malyala P, Cheng CJ, Rajeev KG, Rohde E, Bellinger AM, Kathiresan S. 2021. In vivo
912 CRISPR base editing of PCSK9 durably lowers cholesterol in primates. *Nature* **593**.
913 doi:10.1038/s41586-021-03534-y
914 Niu W, Zang T, Smith DK, Vue TY, Zou Y, Bachoo R, Johnson JE, Zhang CL. 2015. SOX2
915 reprograms resident astrocytes into neural progenitors in the adult brain. *Stem Cell*
916 *Reports* **4**. doi:10.1016/j.stemcr.2015.03.006
917 Niu W, Zang T, Zou Y, Fang S, Smith DK, Bachoo R, Zhang CL. 2013. In vivo

918 reprogramming of astrocytes to neuroblasts in the adult brain. *Nat Cell Biol* **15**.
919 doi:10.1038/ncb2843
920 Niu Y, Moghimyfiroozabad S, Moghimyfiroozabad A, Tierney TS, Alavian KN. 2021. The
921 factors for the early and late development of midbrain dopaminergic neurons segregate
922 into two distinct evolutionary clusters. *Brain Disord* **1**:100002.
923 doi:10.1016/J.DSCB.2021.100002
924 Olsson M, Nikkhah G, Bentlage C, Björklund A. 1995. Forelimb akinesia in the rat Parkinson
925 model: Differential effects of dopamine agonists and nigral transplants as assessed by a
926 new stepping test. *J Neurosci* **15**. doi:10.1523/jneurosci.15-05-03863.1995
927 Paxinos G, Franklin KBJ. 2001. The Mouse Brain in Stereotaxic Coordinates, 2nd edition.
928 *Acad Press*.
929 Qian C, Dong B, Wang XY, Zhou FQ. 2021. In vivo glial trans-differentiation for neuronal
930 replacement and functional recovery in central nervous system. *FEBS J* **288**:4773–4785.
931 doi:10.1111/FEBS.15681
932 Qian H, Kang X, Hu J, Zhang D, Liang Z, Meng F, Zhang X, Xue Y, Maimon R, Dowdy SF,
933 Devaraj NK, Zhou Z, Mobley WC, Cleveland DW, Fu XD. 2020. Reversing a model of
934 Parkinson's disease with in situ converted nigral neurons. *Nature*. doi:10.1038/s41586-
935 020-2388-4
936 Radhiyanti PT, Konno A, Matsuzaki Y, Hirai H. 2021. Comparative study of neuron-specific
937 promoters in mouse brain transduced by intravenously administered AAV-PHP.eB.
938 *Neurosci Lett* **756**:135956. doi:10.1016/J.NEULET.2021.135956
939 Robel S, Berninger B, Götz M. 2011. The stem cell potential of glia: Lessons from reactive
940 gliosis. *Nat Rev Neurosci*. doi:10.1038/nrn2978
941 Rothgangl T, Dennis MK, Lin PJC, Oka R, Witzigmann D, Villiger L, Qi W, Hruzova M,
942 Kissling L, Lenggenhager D, Borrelli C, Egli S, Frey N, Bakker N, Walker JA, Kadina
943 AP, Victorov D V., Pacesa M, Kreutzer S, Kontarakis Z, Moor A, Jinek M, Weissman
944 D, Stoffel M, van Boxtel R, Holden K, Pardi N, Thöny B, Häberle J, Tam YK, Semple
945 SC, Schwank G. 2021. In vivo adenine base editing of PCSK9 in macaques reduces
946 LDL cholesterol levels. *Nat Biotechnol*. doi:10.1038/s41587-021-00933-4
947 Schindelin J, Arganda-Carreras I, Frise E, Kaynig V, Longair M, Pietzsch T, Preibisch S,
948 Rueden C, Saalfeld S, Schmid B, Tinevez JY, White DJ, Hartenstein V, Eliceiri K,
949 Tomancak P, Cardona A. 2012. Fiji: An open-source platform for biological-image
950 analysis. *Nat Methods*. doi:10.1038/nmeth.2019
951 Shimada IS, LeComte MD, Granger JC, Quinlan NJ, Spees JL. 2012. Self-renewal and

952 differentiation of reactive astrocyte-derived neural stem/progenitor cells isolated from
953 the cortical peri-infarct area after stroke. *J Neurosci* **32**. doi:10.1523/JNEUROSCI.4303-
954 11.2012
955 Shin HY, Wang C, Lee HK, Yoo KH, Zeng X, Kuhns T, Yang CM, Mohr T, Liu C,
956 Hennighausen L. 2017. CRISPR/Cas9 targeting events cause complex deletions and
957 insertions at 17 sites in the mouse genome. *Nat Commun*. doi:10.1038/ncomms15464
958 Sirko S, Behrendt G, Johansson PA, Tripathi P, Costa MR, Bek S, Heinrich C, Tiedt S, Colak
959 D, Dichgans M, Fischer IR, Plesnila N, Staufenbiel M, Haass C, Snapyan M,
960 Saghatelyan A, Tsai LH, Fischer A, Grobe K, Dimou L, Götz M. 2013. Erratum:
961 Reactive glia in the injured brain acquire stem cell properties in response to sonic
962 hedgehog (Cell Stem Cell (2013) 12 426-439)). *Cell Stem Cell*.
963 doi:10.1016/j.stem.2013.04.007
964 Stirling DR, Swain-Bowden MJ, Lucas AM, Carpenter AE, Cimini BA, Goodman A. 2021.
965 CellProfiler 4: improvements in speed, utility and usability. *BMC Bioinformatics* **22**.
966 doi:10.1186/s12859-021-04344-9
967 Stoker TB, Barker RA. 2020. Recent developments in the treatment of Parkinson's Disease.
968 *F1000Research* **9**. doi:10.12688/F1000RESEARCH.25634.1
969 Sun H, Monenschein H, Schiffer HH, Reichard HA, Kikuchi S, Hopkins M, Macklin TK,
970 Hitchcock S, Adams M, Green J, Brown J, Murphy ST, Kaushal N, Collia DR, Moore S,
971 Ray WJ, English NM, Carlton MBL, Brice NL. 2021. First-Time Disclosure of
972 CVN424, a Potent and Selective GPR6 Inverse Agonist for the Treatment of Parkinson's
973 Disease: Discovery, Pharmacological Validation, and Identification of a Clinical
974 Candidate. *J Med Chem* **64**. doi:10.1021/acs.jmedchem.0c02081
975 Torper O, Götz M. 2017. Brain repair from intrinsic cell sources: Turning reactive glia into
976 neuronsProgress in Brain Research. doi:10.1016/bs.pbr.2016.12.010
977 Truong DJJ, Kühner K, Kühn R, Werfel S, Engelhardt S, Wurst W, Ortiz O. 2015.
978 Development of an intein-mediated split-Cas9 system for gene therapy. *Nucleic Acids*
979 *Res*. doi:10.1093/nar/gkv601
980 Tsai SQ, Topkar V V., Joung JK, Aryee MJ. 2016. Open-source guideseq software for
981 analysis of GUIDE-seq data. *Nat Biotechnol 2016 345* **34**:483–483.
982 doi:10.1038/nbt.3534
983 Tsai SQ, Zheng Z, Nguyen NT, Liebers M, Topkar V V., Thapar V, Wyvekens N, Khayter C,
984 Iafrate AJ, Le LP, Aryee MJ, Joung JK. 2014. GUIDE-seq enables genome-wide
985 profiling of off-target cleavage by CRISPR-Cas nucleases. *Nat Biotechnol 2014 332*

986 **33**:187–197. doi:10.1038/nbt.3117
987 Valcárcel J, Gebauer F. 1997. Post-transcriptional regulation: The dawn of PTB. *Curr Biol* **7**.
988 doi:10.1016/s0960-9822(06)00361-7
989 Villiger L, Grisch-Chan HM, Lindsay H, Ringnalda F, Pogliano CB, Allegri G, Fingerhut R,
990 Häberle J, Matos J, Robinson MD, Thöny B, Schwank G. 2018. Treatment of a
991 metabolic liver disease by in vivo genome base editing in adult mice. *Nat Med*.
992 doi:10.1038/s41591-018-0209-1
993 Wang LL, Serrano C, Zhong X, Ma S, Zou Y, Zhang CL. 2021. Revisiting astrocyte to
994 neuron conversion with lineage tracing in vivo. *Cell* **184**. doi:10.1016/j.cell.2021.09.005
995 Winter J, Luu A, Gapinske M, Manandhar S, Shirguppe S, Woods WS, Song JS, Perez-
996 Pinera P. 2019. Targeted exon skipping with AAV-mediated split adenine base editors.
997 *Cell Discov* **5**. doi:10.1038/s41421-019-0109-7
998 Xue Y, Ouyang K, Huang J, Zhou Y, Ouyang H, Li H, Wang G, Wu Q, Wei C, Bi Y, Jiang
999 L, Cai Z, Sun H, Zhang K, Zhang Y, Chen J, Fu XD. 2013. Direct conversion of
1000 fibroblasts to neurons by reprogramming PTB-regulated MicroRNA circuits. *Cell*.
1001 doi:10.1016/j.cell.2012.11.045
1002 Xue Y, Qian H, Hu J, Zhou B, Zhou Y, Hu X, Karakhanyan A, Pang Z, Fu XD. 2016.
1003 Sequential regulatory loops as key gatekeepers for neuronal reprogramming in human
1004 cells. *Nat Neurosci 2016 196* **19**:807–815. doi:10.1038/nn.4297
1005 Yang G, Yan Z, Wu X, Zhang M, Xu C, Shi L, Yang H, Fang K. 2023. Ptbp1 knockdown
1006 failed to induce astrocytes to neurons in vivo. *Gene Ther 2023* 1–6. doi:10.1038/s41434-
1007 023-00382-5
1008 Yu GL, Zhang Y, Ning B. 2021. Reactive Astrocytes in Central Nervous System Injury:
1009 Subgroup and Potential Therapy. *Front Cell Neurosci*. doi:10.3389/fncel.2021.792764
1010 Yu X, Nagai J, Khakh BS. 2020. Improved tools to study astrocytes. *Nat Rev Neurosci*.
1011 doi:10.1038/s41583-020-0264-8
1012 Zheng S, Gray EE, Chawla G, Porse BT, O'Dell TJ, Black DL. 2012. Psd-95 is post-
1013 transcriptionally repressed during early neural development by PTBP1 and PTBP2. *Nat*
1014 *Neurosci* **15**:381. doi:10.1038/NN.3026
1015 Zhou H, Su J, Hu X, Zhou C, Li H, Chen Z, Xiao Q, Wang B, Wu W, Sun Y, Zhou Y, Tang
1016 C, Liu F, Wang L, Feng C, Liu M, Li S, Zhang Y, Xu H, Yao H, Shi L, Yang H. 2020.
1017 Glia-to-Neuron Conversion by CRISPR-CasRx Alleviates Symptoms of Neurological
1018 Disease in Mice. *Cell*. doi:10.1016/j.cell.2020.03.024
1019

Figures and figure supplements

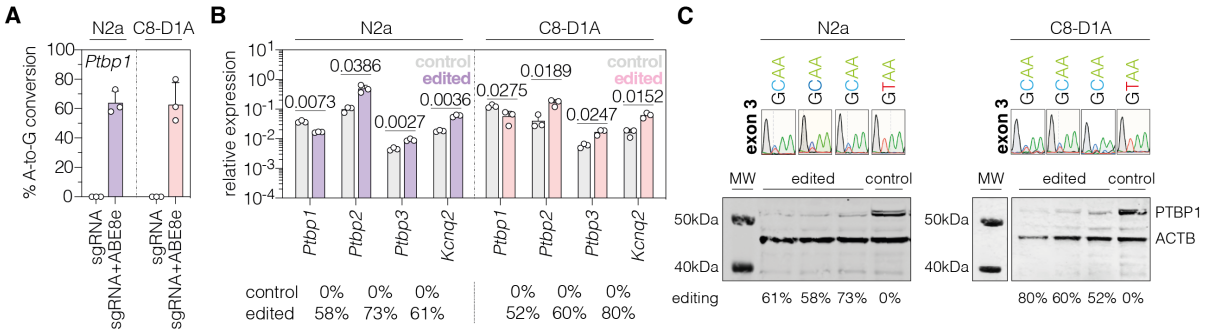

Figure 1 | PTBP1 downregulation by adenine base editing with sgRNA-ex3 in neuronal and astroglial cell lines. (A) Editing rates at the *Ptbp1* splice donor of exon 3 in N2a and C8-D1A cell lines. Editing efficiencies were determined by Sanger sequencing and EditR (Kluesner et al., 2018). Control samples were transfected with sgRNA (gray). **(B)** Transcript levels of *Ptbp1* and *Ptbp1*-repressed exons upon adenine base editing in N2a and C8-D1A cells. Transcripts were normalized to *Gapdh*. **(C)** PTBP1 levels in control (1 independent experiment) and edited N2a or C8-D1A cells (3 independent experiments). ACTB protein levels are shown as a loading control. Corresponding sequencing chromatograms for sgRNA-ex3 are shown above each sample. Corresponding editing rates are shown below the plots in (B) and (C). Normal distribution of the data was analyzed using the Shapiro-Wilk test. Data are represented as means±s.d. of three independent experiments (A,B) and were analyzed using an unpaired two-tailed Student's t-test with Welch's correction (B). Each datapoint represents one independent experiment. Exact *P*-values are indicated in the respective plots. *Ptbp1*, Polypyrimidine tract binding protein 1; *Ptbp2*, Polypyrimidine tract binding protein 2; *Ptbp3*, Polypyrimidine tract binding protein 3; *Kcnq2*, potassium voltage-gates channel subfamily Q member 2; MW, molecular weight marker; kDa, kilodalton.

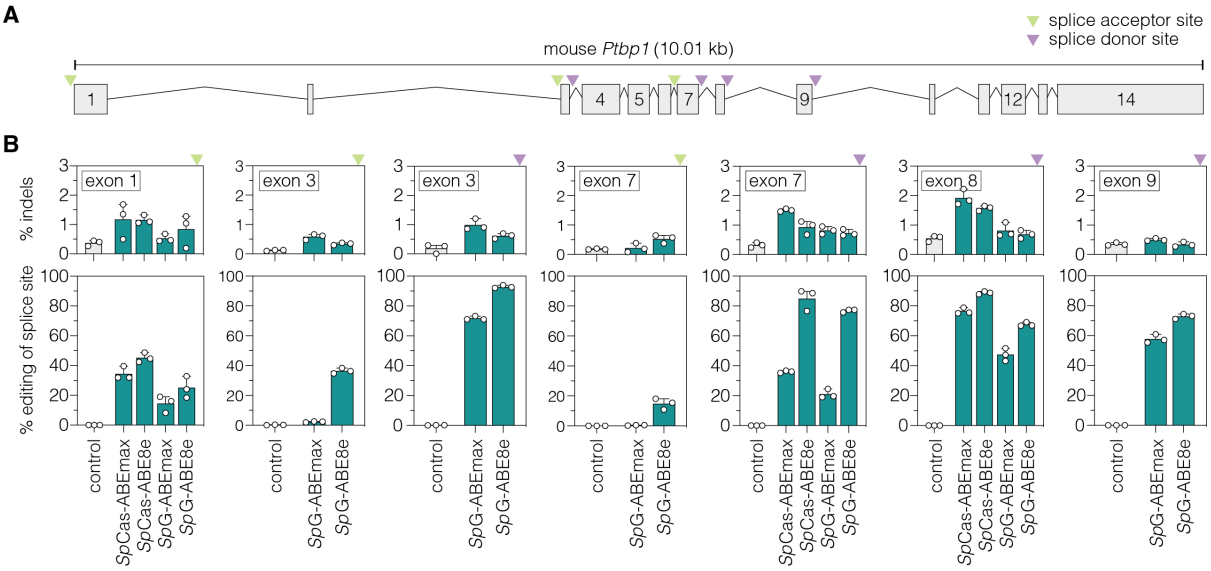

Figure 1 – figure supplement 1 | Adenine base editing of *Ptbp1* splice sites in murine Hepa cells. (A) Schematic overview of exons and introns of the targeted murine *Ptbp1* locus. sgRNAs target either the conserved GT motif of canonical splice donor sites at the beginning of an intron (purple arrowhead) or the conserved AG motif of canonical splice acceptor sites at the end of an intron (green arrowhead). **(B)** Editing of adenines and indel rates at *Ptbp1* splice donor (purple arrowhead) or acceptor sites (green arrowhead) for *Sp*Cas- or *Sp*G-ABE variants (teal). The targeted exons are indicated in the respective plot. Control samples were transfected with sgRNA (gray). Data are displayed as means±s.d. of three independent experiments. Each datapoint represents one independent experiment. *Ptbp1*, polypyrimidine tract binding protein 1; kb, kilobases; *Sp*Cas, *Streptococcus pyogenes* Cas9 recognizing NGG PAMs; *Sp*G, *Sp*Cas variant recognizing NGN PAMs.

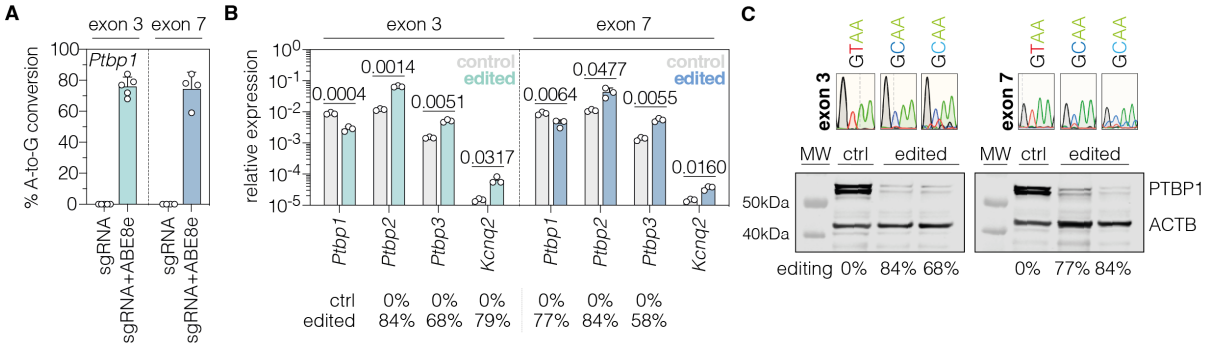

Figure 1 – figure supplement 2 | *In vitro* validation of PTBP1 repression by adenine base editing with sgRNA-ex3 or sgRNA-ex7 in Hepa cells. (A) Editing rates at *Ptbp1* splice donor sites of exon 3 and exon 7. Editing efficiencies were determined by Sanger sequencing and EditR (Kluesner et al., 2018). Control samples were transfected with sgRNA (gray). **(B)** Transcript levels of *Ptbp1* and *Ptbp1*-repressed exons upon adenine base editing in Hepa cells. Transcripts were normalized to *Gapdh*. **(C)** PTBP1 levels in control (1 independent experiment) and edited Hepa cells (2 independent experiments). ACTB protein levels are shown as a loading control. Corresponding sequencing chromatograms for sgRNA-ex3 and sgRNA-ex7 are shown above each sample. Corresponding editing rates are shown below the plots in (B) and (C). Normal distribution of the data was analyzed using the Shapiro-Wilk test. Data are represented as means±s.d. of at least three independent experiments (A,B) and were analyzed using an unpaired two-tailed Student's t-test with Welch's correction (B). Each datapoint represents one independent experiment. Exact *P*-values are indicated in the respective plots. *Ptbp1*, Polypyrimidine tract binding protein 1; *Ptbp2*, Polypyrimidine tract binding protein 2; *Ptbp3*, Polypyrimidine tract binding protein 3; *Kcnq2*, potassium voltage-gates channel subfamily Q member 2; ctrl, control; MW, molecular weight marker.

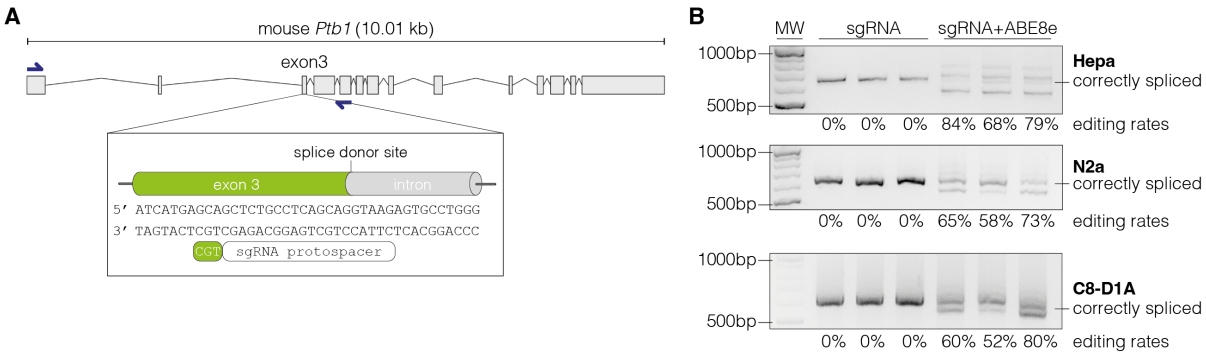

Figure 1 – figure supplement 3 | Adenine base editing generates alternative *Ptbp1* splice sites in cell lines. (A) Schematic representation of the splice donor at the exon-intron junction of *Ptbp1* exon 3. **(B)** Editing of the canonical splice donor at exon 3 generates alternative *Ptbp1* splice sites in Hepa, N2a, and C8-D1A cells. The correctly spliced isoform is labelled. The corresponding editing rates are shown below each plot. Data of three independent experiments are shown (B). Size of molecular weight (MW) markers in basepairs (bp) are indicated in (B).

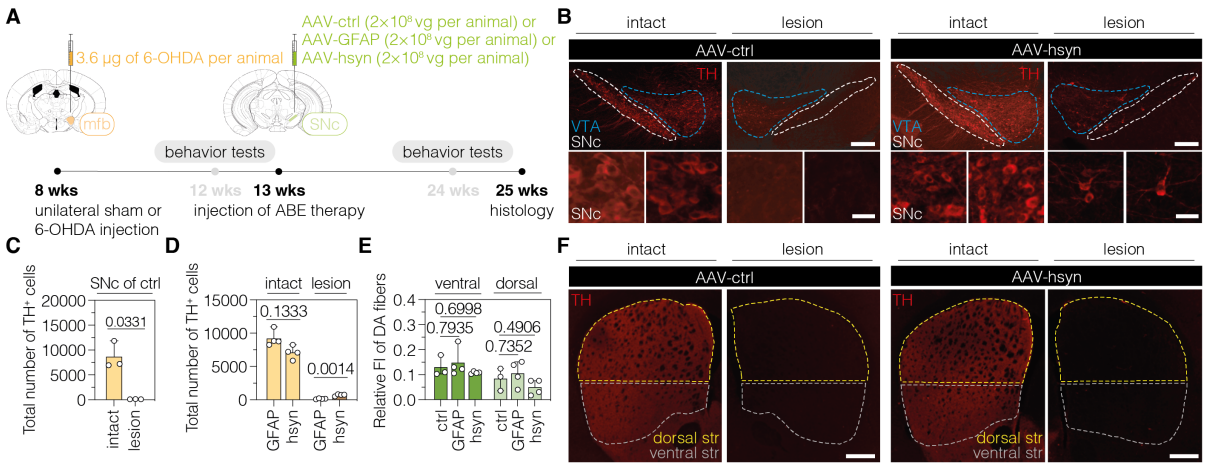

Figure 2 | Downregulation of PTBP1 in neurons of the SNc generates TH$^+$ cells. (A) Schematic representation of the experimental timeline and setup. **(B)** Representative images of midbrain sections showing the intact (left) or lesioned (right) SNc in animals treated with AAV-ctrl (left) or AAV-hsyn (right). Treatment groups and hemispheres are indicated on top. **(C,D)** Quantification of TH$^+$ cells in the intact or lesioned SNc in animals treated with AAV-ctrl (C), AAV-GFAP (D), or AAV-hsyn (D) in the lesioned hemisphere. **(E,F)** Quantifications (E) of DA fibers in the striatum, assessed as relative fluorescence intensity (FI) of TH compared to the intact striatum of the same section, and representative images of brain sections (F) showing the intact or denervated striatum (str) in animals treated with AAV-ctrl (left) or AAV-hsyn (right). The FI of the TH staining detected in the corpus callosum of each hemisphere was used for background correction of FI detected in the striatum of the same hemisphere. Control animals were treated with AAV-PHP.eB particles, expressing the ABE8e variant under the ubiquitous Cbh promoter. Tissue areas used for quantifications are marked by colored dashed lines in (B) and (E). Normal distribution of the data was analyzed using the Shapiro-Wilk test. Data are represented as means±s.d. of 3-8 animals per group and were analyzed using an unpaired two-tailed Student's t-test with Welch's correction (C, D) or a one-way ANOVA with Dunnett's multiple comparisons test (E). Each datapoint represents one animal. Exact *P*-values are indicated in the respective plots. Scale bars, 20 µm (B, bottom) and 1000 µm (B, top; F). ctrl, AAV-ctrl-ABE treatment; GFAP, AAV-GFAP-ABE treatment; hsyn, AAV-hsyn-ABE treatment; ABE, adenine base editor; vg, vector genomes; SNc, substantia nigra pars compacta; VTA, ventral tegmental area; TH, tyrosine hydroxylase; str, striatum; FI, fluorescence intensity; DA, dopaminergic.

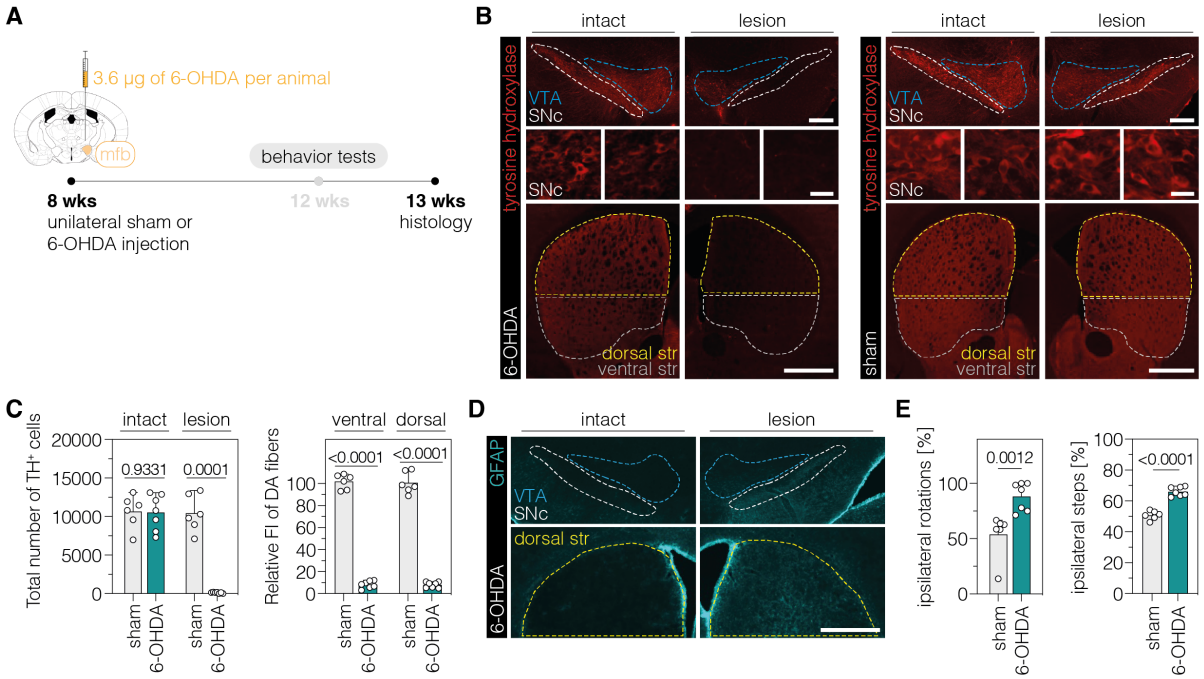

Figure 2 – figure supplement 1 | Validation of the unilateral 6-OHDA lesion in C57BL/6J mice. (A) Schematic representation of the experimental timeline and setup. **(B)** Representative fluorescence images showing the unilateral loss of TH^+ cells in the SNc (top and middle) and unilateral depletion of DA fibers in the striatum (bottom) in 6-OHDA-lesioned mice (left). Sham-injected animals (right) are shown for comparison. The FI of the TH staining detected in the corpus callosum of each hemisphere was used for background correction of FI detected in the striatum of the same hemisphere. Treatment groups are indicated on the left. **(C)** Quantifications of TH^+ DANs in the SNc (left) and DA fibers in the ventral and dorsal striatum (right). Tissue areas used for quantifications are marked by colored dashed lines in (B). **(D)** Unilateral activation of astrocytes in the SNc (top) and dorsal striatum (bottom) in 6-OHDA-lesioned mice. **(E)** Spontaneous behaviors in sham- and 6-OHDA-lesioned mice. Normal distribution of the data was analyzed using the Shapiro-Wilk test. Data are displayed as means±s.d. of 6-7 mice per group and were analyzed using an unpaired two-tailed Student's t-test with Welch's correction (C, ipsilateral steps in E) or a two-tailed Mann Whitney test (ipsilateral rotations in E). Each datapoint represents one animal. Exact *P*-values are indicated in the respective plots. Scale bars, 20 µm (B, bottom) and 1000 µm (B, top; D). FI, fluorescence intensity; SNc, substantia nigra pars compacta; str, striatum; VTA, ventral tegmental area; GFAP, glial fibrillary acidic protein; TH, tyrosine hydroxylase; DA, dopaminergic.

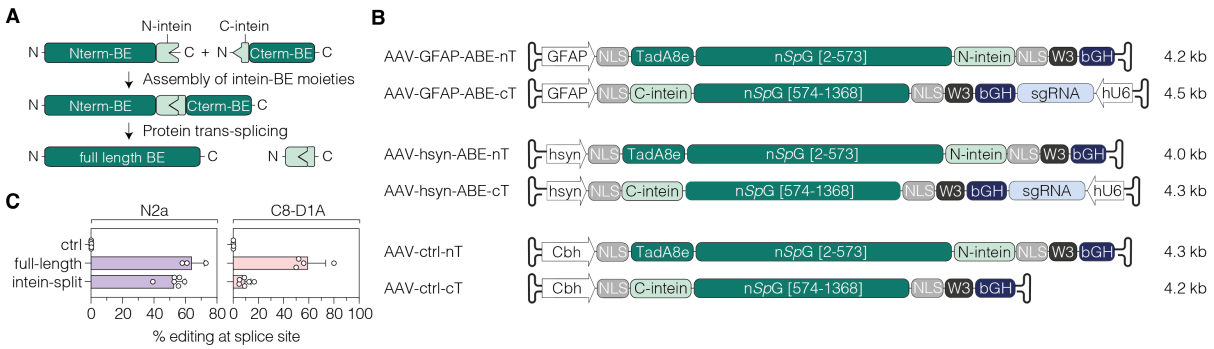

Figure 2 – figure supplement 2 | AAV vector designs for neuronal or astroglial expression of intein-split ABE8e. (A) Depiction of *Npu* intein-split BE moieties (Nterm-BE and Cterm-BE), forming the full length BE after protein trans-splicing. **(B)** Schematic representation of AAV vector designs with the short GFAP (Lee et al., 2008), hsyn (Kügler et al., 2003), or Cbh promoter (Gray et al., 2011) and their corresponding lengths in kilobase pairs (including ITRs). Constructs are not depicted to scale. **(C)** Editing efficiencies of full-length (CMV promoter) or intein-split ABE expression vectors in N2a (hsyn promoter) and C8-D1A cells (GFAP promoter). Control samples were treated with the sgRNA only. Data of 3-6 independent experiments are displayed as means±s.d. (C). BE, base editor; ABE, adenine base editor; nT/Nterm, N-terminal AAV construct; cT/Cterm, C-terminal AAV construct; GFAP, glial fibrillary acidic protein promoter; hsyn, human synapsin 1 promoter; Cbh, truncated chimeric CMV/chicken b-actin hybrid promoter; NLS, nuclear localization signal; TadA8e, adenosine deaminase; n*Sp*G, *Sp*G nickase; W3, woodchuck hepatitis virus post-transcriptional regulatory element; bGH, bovine growth hormone poly adenylation signal; hU6, human U6 promoter; kb, kilobase pairs.

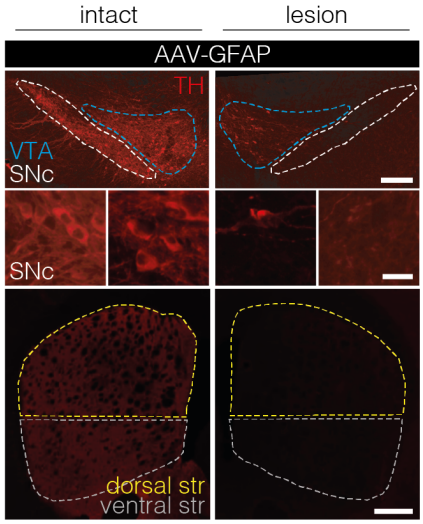

Figure 2 - figure supplement 3 | PTBP1 downregulation in astrocytes of the SNc fails to generate TH$^+$ cells. Representative images of brain sections showing the intact (left) or lesioned (right) SNc (top and middle) or striatum (bottom) in animals after astroglial PTBP1 downregulation (n=4 mice). The FI of the TH staining detected in the corpus callosum of each hemisphere was used for background correction of FI detected in the striatum of the same hemisphere. Tissue areas used for quantifications are marked by colored dashed lines. Scale bars, 20 µm (middle) and 1000 µm (top and bottom). AAV-GFAP, AAV-GFAP-ABE treatment; GFAP, glial fibrillary acidic protein; SNc, substantia nigra pars compacta; VTA, ventral tegmental area; TH, tyrosine hydroxylase.

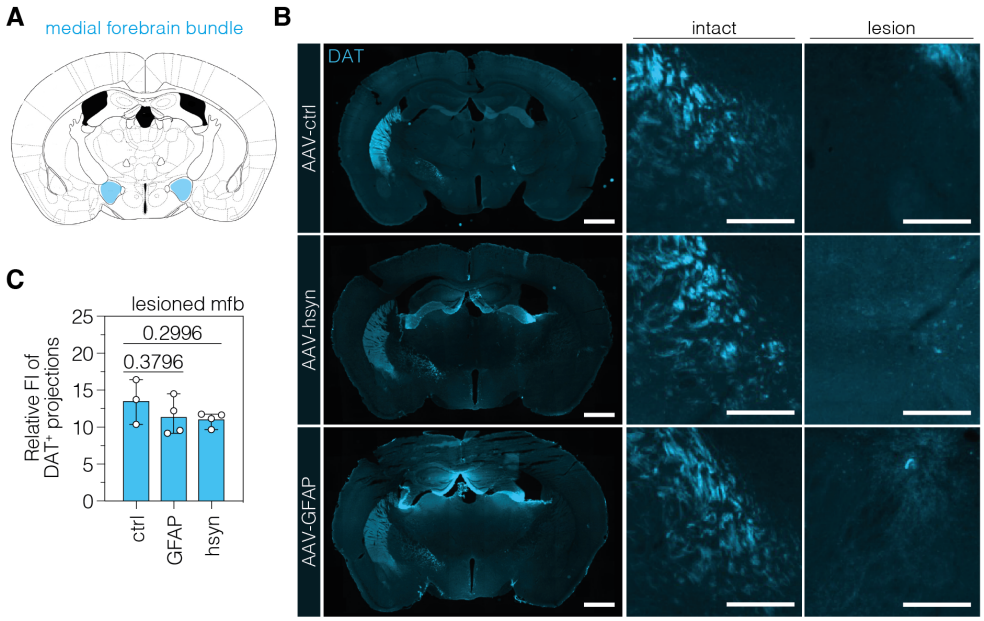

Figure 2 - figure supplement 4 | TH-expressing cells in the SNc do not form neuronal projections through the mfb. (A,B) Schematic depiction of the mfb (A) on the mouse brain atlas (Paxinos and Franklin, 2001) and representative images of DA projections in the mfb of the intact and lesioned hemisphere in treated PD mice. Treatment groups (left) and hemispheres (top) are indicated. **(C)** Quantifications of DA projections in the mfb, assessed as relative fluorescence intensity (FI) of the dopaminergic marker DAT (dopamine transporter) compared to the intact mfb of the same section, in animals treated with AAV-ctrl, AAV-GFAP, or AAV-hsyn. The FI of the DAT staining detected in the thalamus of each hemisphere was used for background correction of FI detected in the mfb of the same hemisphere. Control animals were treated with AAV-PHP.eB particles, expressing the ABE8e variant under the ubiquitous Cbh promoter. Normal distribution of the data was analyzed using the Shapiro-Wilk test. Data are represented as means±s.d. of 3-4 animals per group and were analyzed using a one-way ANOVA with Dunnett's multiple comparisons test. Each datapoint represents one animal. Exact *P*-values are indicated in the respective plots. Scale bars, 1000 µm (left) and 50 µm (middle and right). ctrl, AAV-ctrl-ABE treatment; GFAP, AAV-GFAP-ABE treatment; hsyn, AAV-hsyn-ABE treatment; mfb, medial forebrain bundle; FI, fluorescence intensity; DA, dopaminergic; DAT, dopamine transporter.

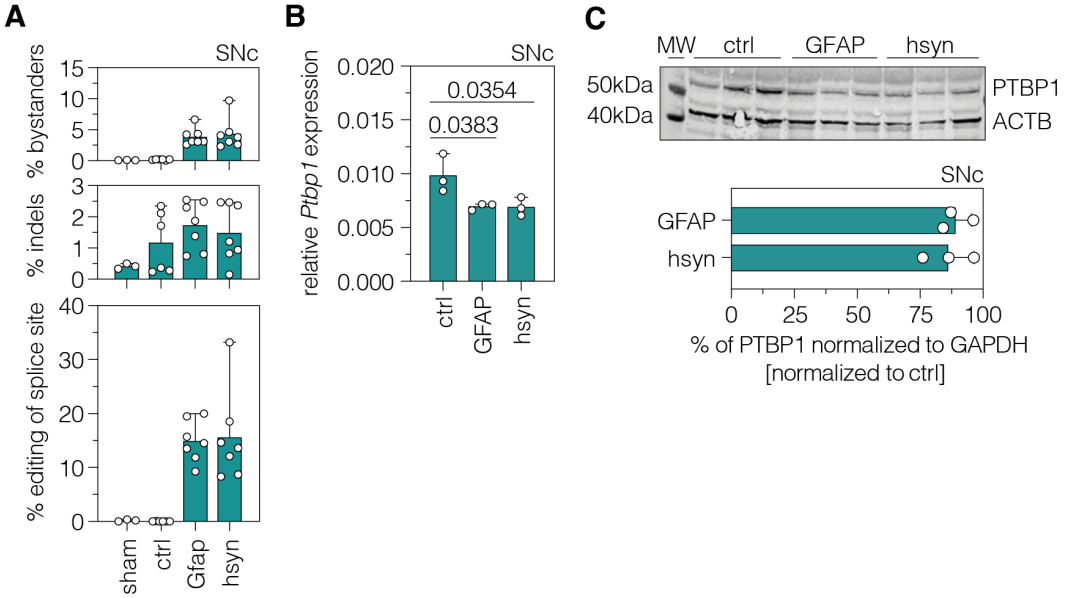

Figure 2 – figure supplement 5 | *In vivo* validation of PTBP1 downregulation by adenine base editing in astrocytes and neurons of the SNc. (A) Quantifications of *in vivo* base editing of adenines and indel rates within the editing window at the targeted *Ptbp1* splice donor. **(B)** Transcript levels of *Ptbp1* upon adenine base editing in the lesioned SNc of AAV-ctrl-, AAV-GFAP-, and AAV-hsyn-treated PD mice. Transcripts were normalized to *Gapdh*. **(C)** PTBP1 levels in the lesioned SNc of treated 6-OHDA-lesioned PD mice (n=3 mice per group). ACTB protein levels are shown as a loading control. PTBP1 abundance was compared to ACTB and normalized to the PTBP1/ACTB ratio of AAV-ctrl-treated animals. Control animals were treated with AAV-PHP.eB particles, expressing the ABE8e variant under the ubiquitous Cbh promoter. Normal distribution of the data was analyzed using the Shapiro-Wilk test. Data are represented as means±s.d. of 3-7 animals per group and were analyzed using a one-way ANOVA with Dunnett's multiple comparisons test (C). Each datapoint represents one animal. Exact *P*-values are indicated in the respective plots. ctrl, AAV-ctrl-ABE treatment; GFAP, AAV-GFAP-ABE treatment; hsyn, AAV-hsyn-ABE treatment; SNc, substantia nigra pars compacta; *Ptbp1*/PTBP1, Polypyrimidine tract binding protein 1; ACTB, beta actin; MW, molecular weight marker.

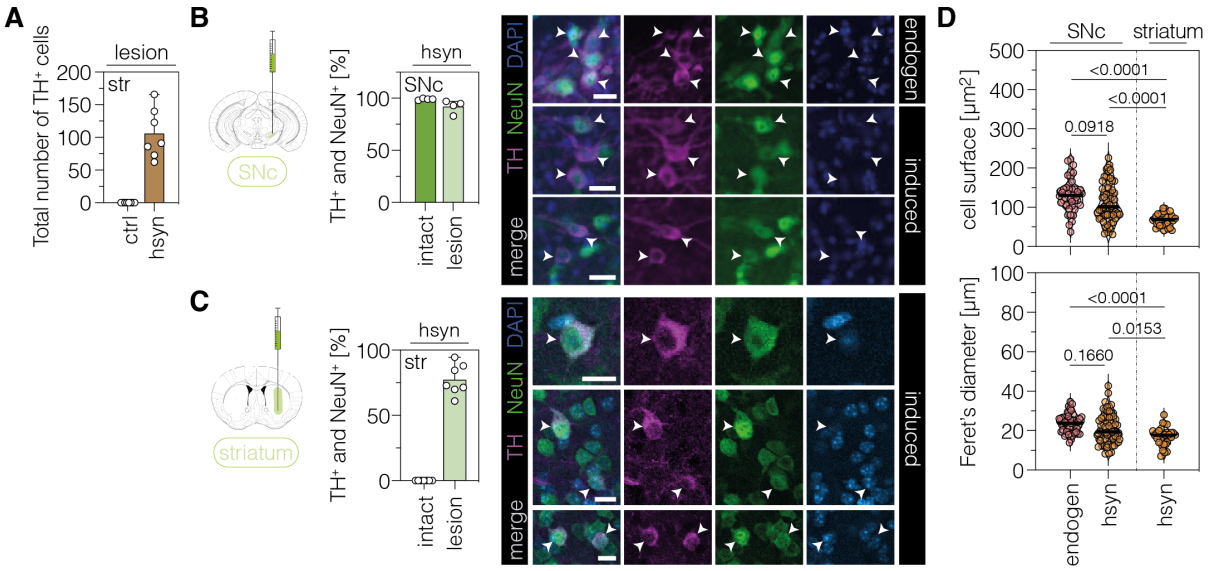

Figure 3 | Characterization of TH-expressing cells in the SNc or striatum. (A) Quantification of TH$^+$ cells in the lesioned striatum of animals treated with AAV-ctrl or AAV-hsyn. Control animals were treated with AAV-PHP.eB particles, expressing the ABE8e-*Sp*G variant under the ubiquitous Cbh promoter. **(B,C)** Quantifications (left) and representative images (right) of TH/NeuN double-positive cell bodies in the intact (dark green, labelled as "endogen" in the images) or lesioned (light green, labelled as "induced" in the images) SNc (B) or striatum (C) of AAV-hsyn-treated animals. **(D)** Corresponding quantifications of cell surface area and Feret's diameter (longest distance between the cell boundaries) of TH/NeuN double-positive cell bodies in the intact (labeled as "endogen") or lesioned SNc or striatum (labeled as "hsyn"). Normal distribution of the data was analyzed using the Shapiro-Wilk test. Data are displayed as means±s.d. of 4-7 mice per group (A-C) or 32-68 TH/NeuN double-positive cells per group (D; n=4 mice) and were analyzed using a one-way ANOVA with Tukey's multiple comparisons test (D). Each datapoint represents one animal (A-C) or a TH/NeuN double-positive cell (D). Exact *P*-values are indicated in the each plot above the respective group (D). Scale bars, 20 µm. ctrl, AAV-ctrl-ABE treatment; hsyn, AAV-hsyn-ABE treatment; SNc, substantia nigra pars compacta; str, striatum; TH, tyrosine hydroxylase; NEUN, hexaribonucleotide binding protein-3; DAPI, 4',6-diamidino-2-phenylindole; endogen, endogenous.

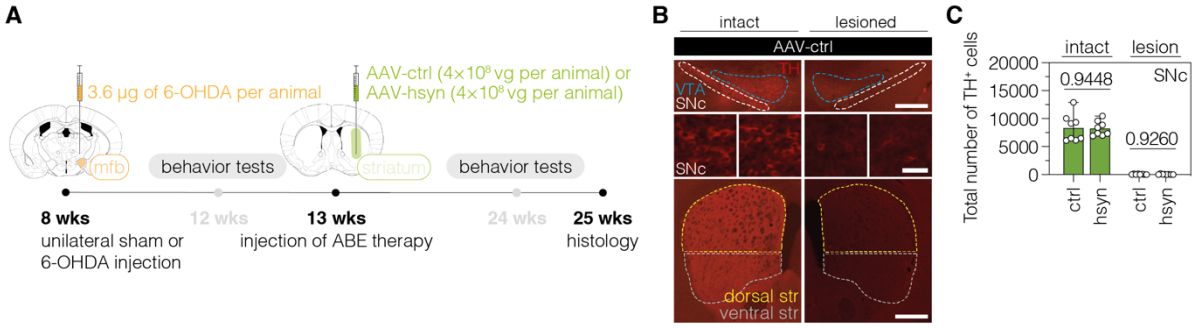

Figure 3 – figure supplement 1 | Validation of the unilateral lesion in 6-OHDA mice after neuronal PTBP1 downregulation in the striatum. (A) Schematic representation of the experimental timeline and setup. **(B)** Representative fluorescence images showing the unilateral loss of TH^+ cells in the SNc (top and middle) and unilateral depletion of DA fibers in the striatum (bottom) in 6-OHDA-lesioned mice treated with AAV-ctrl. Scale bars, 1000 µm (top and bottom) and 20 µm (middle). **(C)** Quantifications of TH^+ cells in the intact (dark green) and lesioned (light green) SNc after administration of the AAV-hsyn treatment to the striatum. Control animals were treated with AAV-PHP.eB particles, expressing the ABE8e-*Sp*G variant under the Cbh promoter. Tissue areas used for quantifications are marked by colored dashed lines in (B). Normal distribution of the data was analyzed using the Shapiro-Wilk test. Data are displayed as means±s.d. of 8 mice per group and were analyzed using an unpaired two-tailed Student's t-test with Welch's correction (C, "intact") or a two-tailed Mann-Whitney test (C, "lesion"). Each datapoint represents one animal. Exact *P*-values are indicated in the respective plots. ABE, adenine base editor; ctrl, AAV-ctrl-ABE treatment; hsyn, AAV-hsyn-ABE treatment; SNc, substantia nigra pars compacta; VTA, ventral tegmental area; TH, tyrosine hydroxylase.

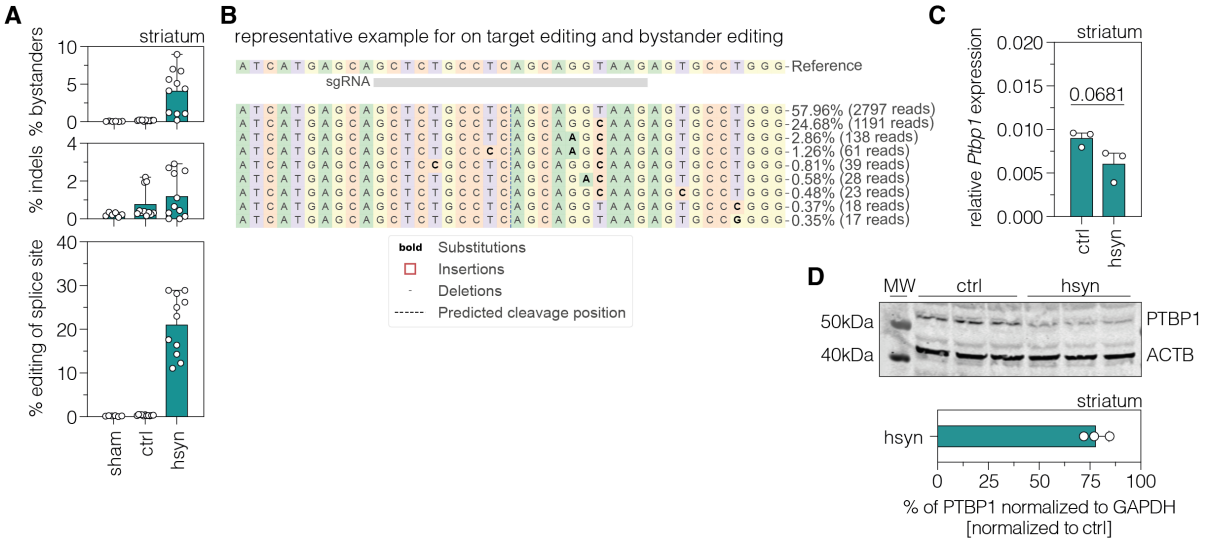

Figure 3 – figure supplement 2 | *In vivo* validation of PTBP1 downregulation by adenine base editing in neurons of the striatum. (A) Quantifications of *in vivo* base editing of adenines and indel rates within the editing window at the targeted *Ptbp1* splice donor (n=6-11 mice per group). **(B)** Representative CRISPResso output file showing the frequency and positioning of edited adenines in the lesioned striatum. **(C)** Transcript levels of *Ptbp1* upon adenine base editing in the lesioned striatum. Transcripts were normalized to *Gapdh* (n=3 mice per group). **(D)** PTBP1 levels in the lesioned striatum of treated 6-OHDA-lesioned PD mice (n=3 mice per group). ACTB protein levels are shown as a loading control. PTBP1 abundance was compared to ACTB and normalized to the PTBP1/ACTB ratio of AAV-ctrl-treated animals. Control animals were treated with AAV-PHP.eB particles, expressing the ABE8e variant under the ubiquitous Cbh promoter. Normal distribution of the data was analyzed using the Shapiro-Wilk test. Data are represented as means±s.d. of 3-11 animals per group and were analyzed using an unpaired two-tailed Student's t-test with Welch's correction (B). Each datapoint represents one animal. Exact *P*-values are indicated in the respective plots. ctrl, AAV-ctrl-ABE treatment; hsyn, AAV-hsyn-ABE treatment; str, striatum; *Ptbp1*/PTBP1, Polypyrimidine tract binding protein 1; ACTB, beta actin; MW, molecular weight marker.

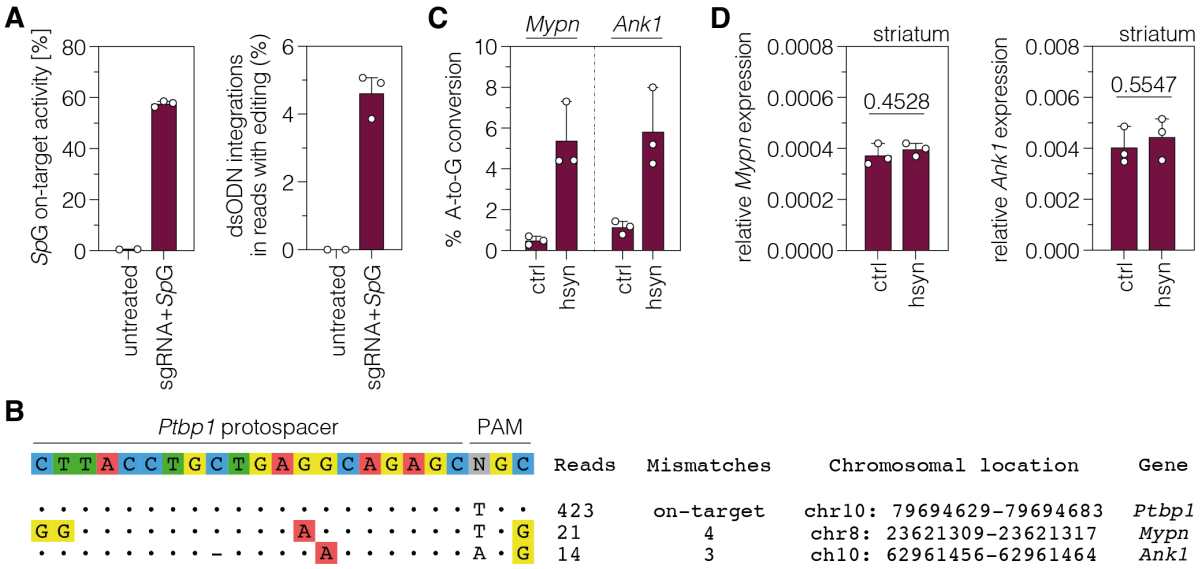

Figure 3 – figure supplement 3 | Identification of sgRNA-dependent off-target sites using GUIDE-seq. (A) Frequency of indels of sgRNA-ex3 and the *Sp*G nuclease (left) and dsODN integrations within the edited reads (right) in N2a cells. **(B)** Experimentally identified off-target sites for the sgRNA-ex3 protospacer targeting the *Ptbp1* locus. The number of reads for the on-target (top) and off-target sites (middle and bottom) as well as the number of mismatches, chromosomal location, and gene annotation are indicated on the right. **(C,D)** Deep sequencing results of the off-target sites (C) and transcript levels (D) of *Mypn* and *Ank1* upon adenine base editing in the lesioned striatum. Transcripts were normalized to *Gapdh* (n=3 mice per group). Data are represented as means±s.d. of 3 animals per group and were analyzed using an unpaired two-tailed Student's t-test with Welch's correction (D).

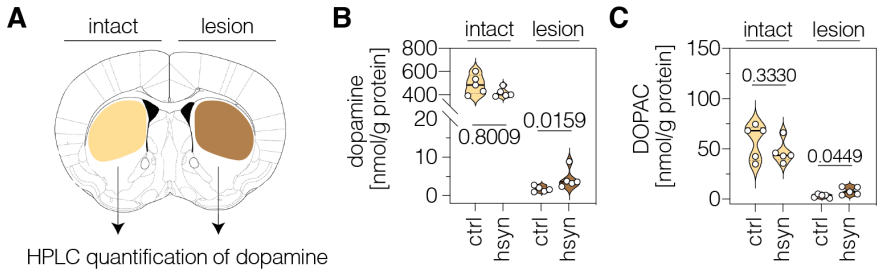

Figure 3 – figure supplement 4 | Neuronal PTBP1 repression in the striatum increases striatal dopamine in 6-OHDA-lesioned hemispheres. (A) Schematic representation of striatal regions used for neurotransmitter quantifications. (**B,C**) HPLC quantifications of dopamine (B) and its metabolite DOPAC (C) in the intact and lesioned striatum of animals treated with AAV-ctrl or AAV-hsyn. Control animals were treated with AAV-PHP.eB particles, expressing the ABE8e-*Sp*G variant under the Cbh promoter. Neurotransmitter concentrations in nmol were normalized to total protein amounts in g. Normal distribution of the data was analyzed using the Shapiro-Wilk test. Data are displayed as means±s.d. of 5 mice per group and were analyzed using an unpaired two-tailed Student's t-test ("intact" in B; C) or a two-tailed Mann-Whitney test ("lesion" in B). Each datapoint represents one animal. Exact *P*-values are indicated in the respective plots. ctrl, AAV-ctrl-ABE treatment; hsyn, AAV-hsyn-ABE treatment; DOPAC, 3,4-dihydroxyphenylacetic acid; nmol, nanomol; g, gram.

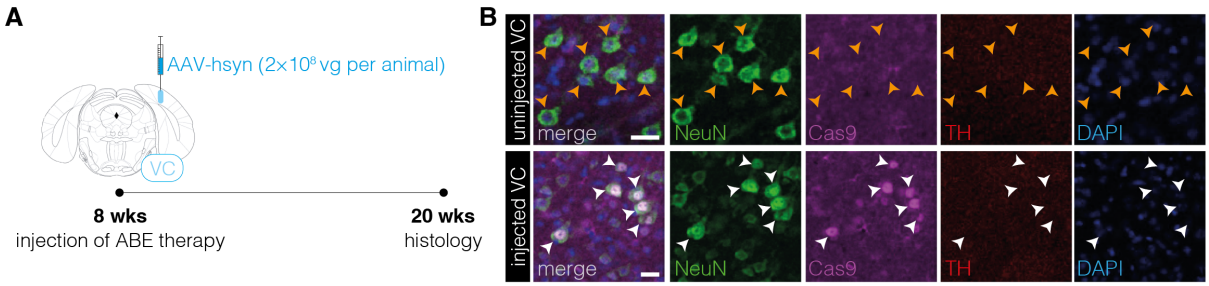

1269

1270 **Figure 3 – figure supplement 5 | Absence of TH$^+$ cell bodies in the visual cortex after**
1271 **neuronal PTBP1 downregulation. (A)** Schematic representation of the experimental timeline
1272 and setup. **(B)** Representative images showing ABE8e expression in neurons (white
1273 arrowheads) of the visual cortex (VC) in the injected hemisphere and absence of TH$^+$ cell
1274 bodies after 12 weeks (bottom). Absence of ABE8e expression in neurons (orange arrowheads)
1275 of the uninjected hemisphere (top) is shown for comparison (n=3 mice). Scale bars, 20μm. VC,
1276 visual cortex; NEUN, hexaribonucleotide binding protein-3; Cas9, *Streptococcus pyogenes*
1277 Cas9; TH, tyrosine hydroxylase; DAPI, 4',6-diamidino-2-phenylindole.

1278

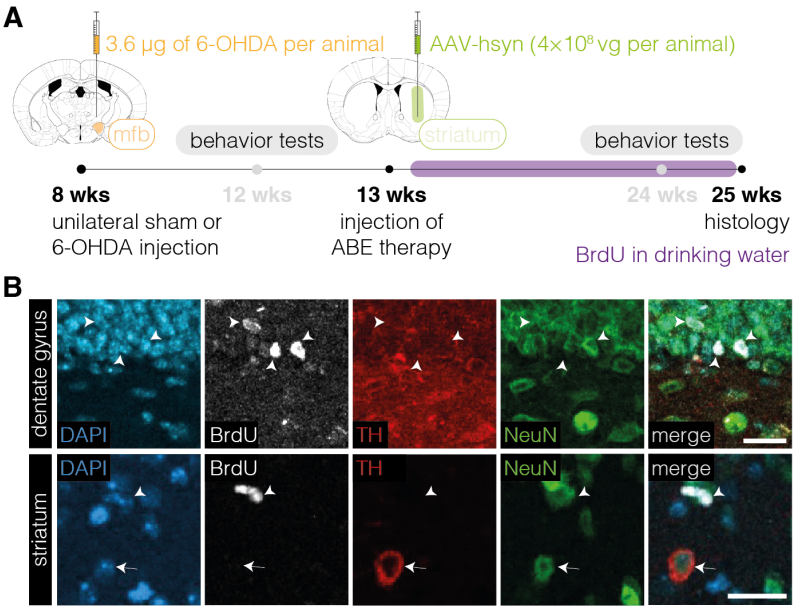

Figure 3 – figure supplement 6 | Absence of proliferation in TH$^+$ cell bodies in the striatum after neuronal PTBP1 downregulation. (A) Schematic representation of the experimental timeline and setup. (**B**) Representative images of BrdU-labeled cells (white arrowhead) in the dentate gyrus (DG, top) or striatum (bottom) and of TH$^+$ cell bodies (white arrow) in the striatum of animals treated with AAV-hsyn (n=4 mice; n=163 TH$^+$ cell bodies in the striatum). Images of the DG are shown as a positive control (top). Scale bars, 20µm. ABE, adenine base editor; DAPI, 4',6-diamidino-2-phenylindole; BrdU, bromodeoxyuridine; TH, tyrosine hydroxylase; NEUN, hexaribonucleotide binding protein-3.

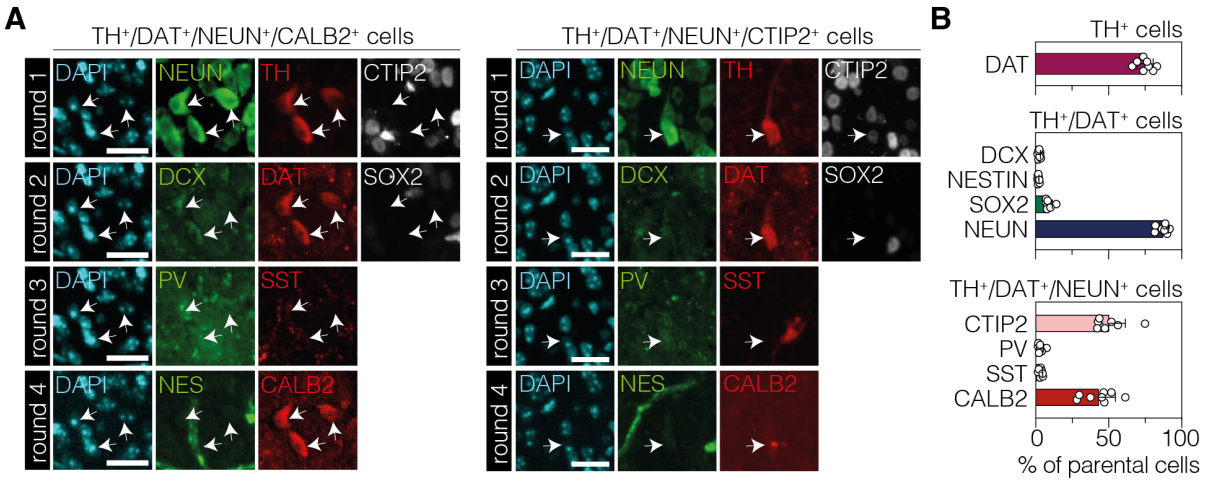

Figure 4 | Characterization of TH$^+$ cells in the striatum after neuronal PTBP1 downregulation. (**A**) Representative 4i images of the two main cell populations among TH-positive cells. The expressed markers are indicated on top of the images. (**B**) Corresponding quantifications of phenotypic markers expressed among TH-positive cells (top, DAT; n=696 TH$^+$ cells), TH/DAT double-positive (middle, DCX; NESTIN; SOX2; n=527 cells), or TH/DAT/NEUN triple-positive (bottom, CTIP2; PV; SST; CALB2; n=460 cells) subpopulations (white arrows) in the striatum at 12 weeks after administration of the AAV-hsyn treatment. The parental population is indicated above each plot. 4i imaging rounds are indicated on the left in (A). Images were pseudocolored during post-processing. Scale bars, 20μm. Data are displayed as means of 6 mice (B). DAPI, 4',6-diamidino-2-phenylindole; SOX2, sex determining region Y-box 2; NES, neuroepithelial stem cell protein; DCX, doublecortin; NEUN, hexaribonucleotide binding protein-3; TH, tyrosine hydroxylase; DAT, dopamine transporter; CTIP2, COUP-TF-interacting protein 2; PV, parvalbumin; SST, somatostatin; CALB2, calbindin 2.

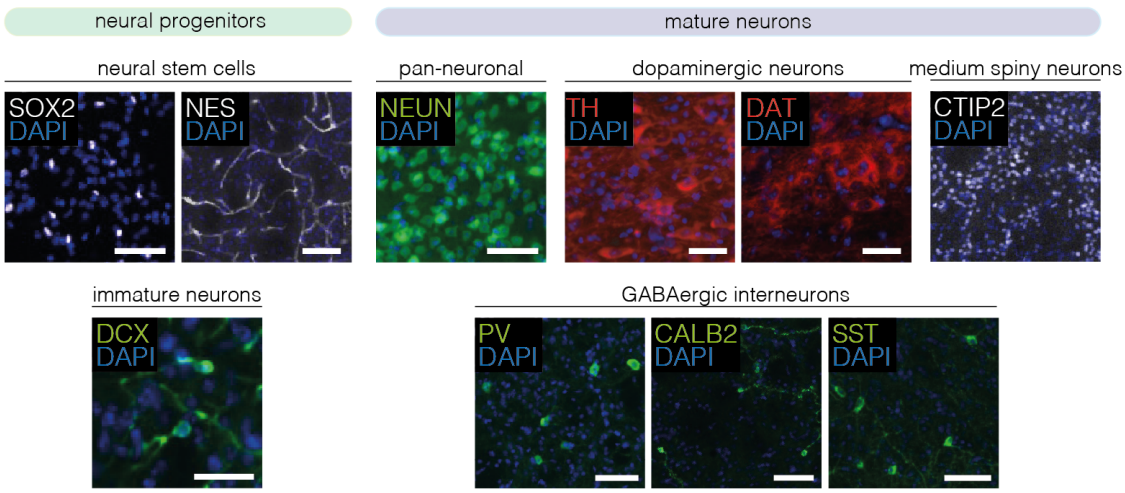

1307

1308 **Figure 4 – figure supplement 1 | Validation of antibodies for 4i experiments.** Antibody
1309 specificity was assessed on mouse brain sections of the striatum or SNc (n=2 animals).
1310 Representative images of one animal are shown. Scale bars, 50μm. DAPI, 4',6-diamidino-2-
1311 phenylindole; SOX2, sex determining region Y-box 2; NES, neuroepithelial stem cell protein;
1312 DCX, doublecortin; NEUN, hexaribonucleotide binding protein-3; TH, tyrosine hydroxylase;
1313 DAT, dopamine transporter; CTIP2, COUP-TF-interacting protein 2; PV, parvalbumin;
1314 CALB2, calbindin 2; SST, somatostatin.

1315

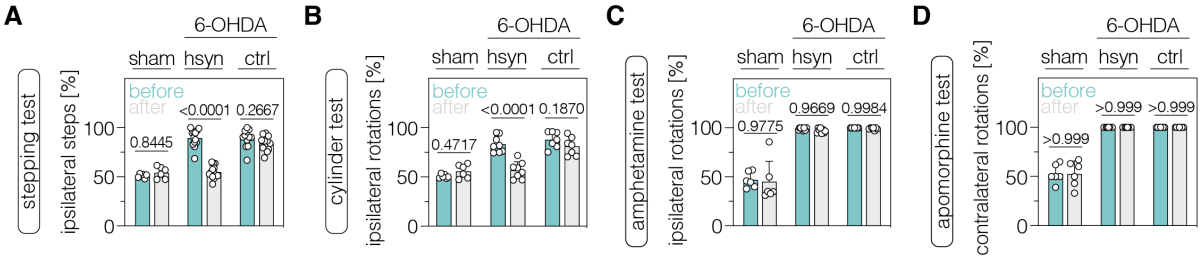

Figure 5 | Neuronal PTBP1 downregulation in the striatum alleviates drug-free motor dysfunction in 6-OHDA-lesioned PD mice. (A,B) Spontaneous behaviors, assessed as contralateral forelimb akinesia in the stepping test (A) and spontaneous rotations in the cylinder test (B), in animals treated in the striatum. (**C,D**) Drug-induced rotations, assessed as amphetamine-induced ipsilateral rotations (C) and apomorphine-induced contralateral rotations (D), in animals treated in the striatum. Normal distribution of the data was analyzed using the Shapiro-Wilk test. Data are represented as means±s.d. of 6-13 animals per group and were analyzed using a two-way ANOVA with Śidák's multiple comparisons. Each datapoint represents one animal. Exact *P*-values are indicated in each plot. hsyn, AAV-hsyn-ABE treatment; ctrl, AAV-ctrl-ABE treatment.

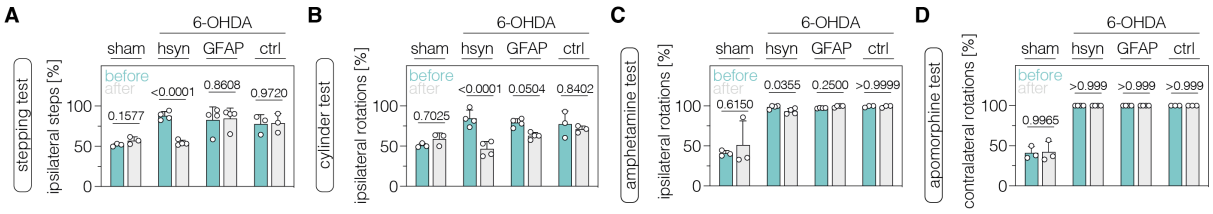

Figure 5 – figure supplement 1 | Neuronal PTBP1 downregulation in the SNc alleviates drug-free motor dysfunction in 6-OHDA-lesioned PD mice. (A,B) Spontaneous behaviors, assessed as contralateral forelimb akinesia in the stepping test (A) and spontaneous rotations in the cylinder test (B), in animals treated in the SNc. (**C,D**) Drug-induced rotations, assessed as amphetamine-induced ipsilateral rotations (C) and apomorphine-induced contralateral rotations (D), in animals treated in the SNc. Normal distribution of the data was analyzed using the Shapiro-Wilk test. Data are represented as means±s.d. of 3-4 animals per group and were analyzed using a two-way ANOVA with Šidák's multiple comparisons test. Each datapoint represents one animal. Exact *P*-values are indicated in each plot. hsyn, AAV-hsyn-ABE treatment; GFAP, AAV-GFAP-ABE treatment; ctrl, AAV-ctrl-ABE treatment.

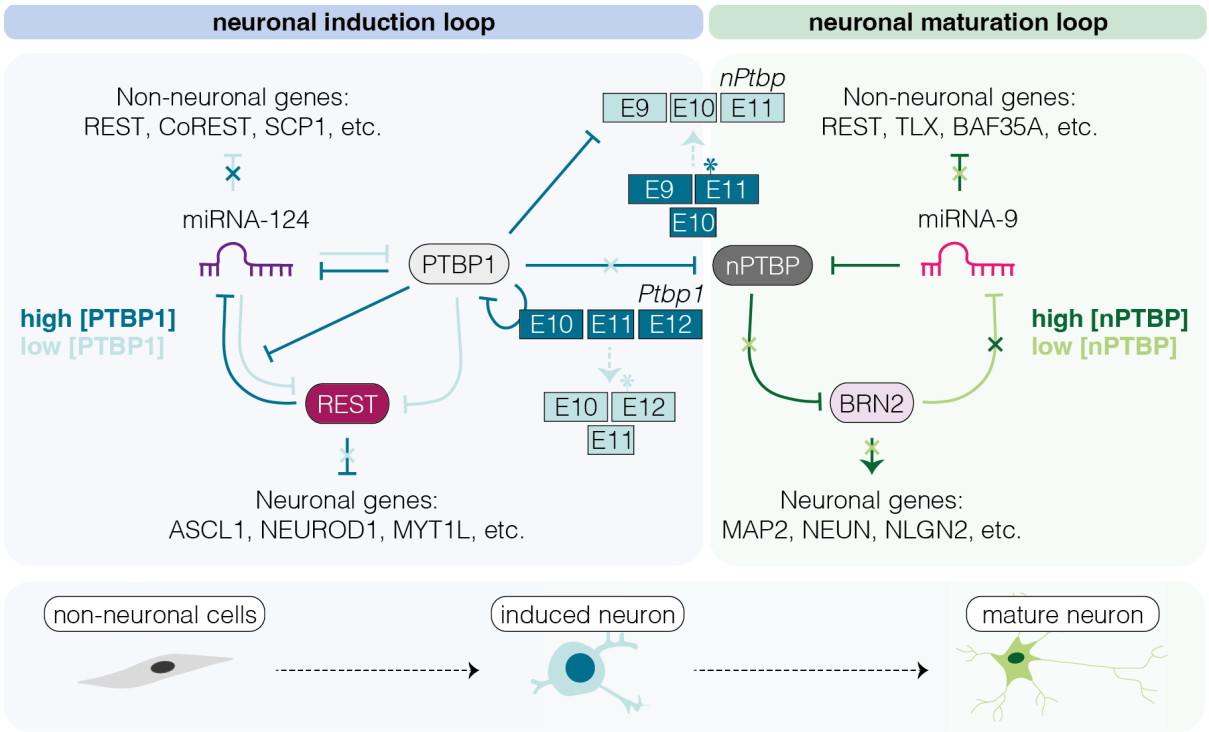

Figure 5 – figure supplement 2 | Schematic representation of the PTBP1/nPTBP regulatory loops driving neuronal differentiation and maturation. The dynamic regulation of PTBP1-mediated inhibition of miRNA-124, which acts on components of the REST complex to activate neuronal-specific expression programs in non-neuronal cells is a key event in the miRNA-124/REST signaling cascade. High PTBP1 expression in non-neuronal cells blocks miRNA-124-induced neuronal differentiation. During neuronal differentiation (low [PTBP1]), miRNA-124 represses PTBP1, enabling expression of nPTBP, pro-neuronal transcription factors, and consequently neuron-specific splicing events that eventually lead to neuronal maturation (Makeyev et al., 2007; Xue et al., 2013).

1351 **Supplementary tables**

1352

1353 Supplementary table 1: Oligos used for cloning of sgRNA plasmids.

oligo name	sgRNA_ID	sequence (5′ → 3′)
sgRNA01_PTBP1_fwd	sgRNA-01	CACCGACTTACCCGTCCATGGCACA
sgRNA01_PTBP1_rev		AAACTGTGCCATGGACGGGTAAGTC
sgRNA02_PTBP1_fwd	sgRNA-02	CACCGCTTACCTGCTGAGGCAGAGC
sgRNA02_PTBP1_rev		AAACGCTCTGCCTCAGCAGGTAAGC
sgRNA03_PTBP1_fwd	sgRNA-03	CACCGTTCTCAGCGGGGATCCGACG
sgRNA03_PTBP1_rev		AAACCGTCGGATCCCCGCTGAGAAC
sgRNA04_PTBP1_fwd	sgRNA-04	CACCGACTCACCAGCTTGGCATGCT
sgRNA04_PTBP1_rev		AAACAGCATGCCAAGCTGGTGAGTC
sgRNA05_PTBP1_fwd	sgRNA-05	CACCGCCCACAGTCCCTGGATGGCC
sgRNA05_PTBP1_rev		AAACGGCCATCCAGGGACTGTGGGC
sgRNA06_PTBP1_fwd	sgRNA-06	CACCGCTTACCAAAGGCTGCTGCCA
sgRNA06_PTBP1_rev		AAACTGGCAGCAGCCTTTGGTAAGC
sgRNA07_PTBP1_fwd	sgRNA-07	CACCGAATACCTGCGGCCTGAGGGA
sgRNA07_PTBP1_rev		AAACTCCCTCAGGCCGCAGGTATTC
sgRNA08_PTBP1_fwd	sgRNA-08	CACCGACATACCTCAGGGTTCAGAT
sgRNA08_PTBP1_rev		AAACATCTGAACCCTGAGGTATGTC

1354

1355 Supplementary table 2: Oligos used for cloning of AAV plasmids.

oligo name	sequence (5′ → 3′)
pGfap-AAV-fwd	CGGCCTCTAGATCAGGGTACCAACATATCCTGGTGTGGAGTAGGG
pGfap-AAV-rev	CGGCCTCTAGATCAGGGTACCAACATATCCTGGTGTGGAGTAGGG
phsyn-AAV-fwd	CGGCCTCTAGATCAGGGTACCGAGGGCCCTGCGTATGAG
phsyn-AAV-rev	CTGTCCGTTTCATGGTGGCACCGGTCCAACTCTCGACTGCGCTC

1356

1357 Supplementary table 3: Oligos used for RT-qPCR.

oligo name	sequence (5′ → 3′)
Gapdh-RTqPCR_fwd	CATCACTGCCACCCAGAAGACTG
Gapdh-RTqPCR_rev	ATGCCAGTGAGCTTCCCGTTCAG
Ptbp1-RTqPCR_fwd	CACCGCTTCAAGAAACCAGGCT
Ptbp1-RTqPCR_rev	GTTGCTGGAGAAGAGGCTCTTG
Ptbp2-RTqPCR_fwd	CCTGTAACACTTGATGTCCTTCAC
Ptbp2-RTqPCR_rev	CACCATACTGGAGCAAAGCCTG
Ptbp3-RTqPCR_fwd	CTCGCTGGTTTCCCGGAG
Ptbp3-RTqPCR_rev	TCCCCGCTTTAAACCGACTG
Kcnq2-RTqPCR_fwd	GTCTTCTCCTGCCTTGTGCT
Kcnq2-RTqPCR_rev	GCAGCCCAGATCCTCACAAA

1358

1359 Supplementary table 4: List of antibodies used in this study.

antibody	clone	host species	dilution	application
NEUN	EPR12763	rabbit	1:1′000	histology, primary
GFAP	ab95231	chicken	1:1′500	histology, primary
TH	na	mouse	1:1′000	histology&4i, primary
TH	ab76442	chicken	1:500	histology, primary
*Sp*Cas9	7A9-3A3	mouse	1:50	histology, primary
BrdU	BU1/75 (ICR1)	rat	1:400	histology, primary
DCX	sc-8066	goat	1:300	4i, primary
Nestin	EPR22023	rabbit	1:100	4i, primary
Sox2	14-9811-82	rat	1:300	4i, primary
DAT	ab184451	rabbit	1:300	4i, primary
CTIP2	25B6	rat	1:500	4i, primary
PV	EPR13091	goat	1:100	4i, primary
SST	G10	mouse	1:250	4i, primary
CALB2	6B3	mouse	1:250	4i, primary
anti-rabbit AF488	JIR-711-545-152	donkey	1:1′000	histology, secondary
anti-rabbit Cy3	JIR-711-165-152	donkey	1:500	histology, secondary

Supplementary table 4 continued.

antibody	clone	host species	dilution	application
anti-chicken Cy5	JIR-703-175-155	donkey	1:500	histology, secondary
anti-mouse Cy3	JIR-715-165-151	donkey	1:500	histology, secondary
anti-goat AF488	JIR-705-545-003	donkey	1:1’000	histology, secondary
anti-goat Cy5	JIR-705-175-147	donkey	1:5000	histology, secondary
anti-rat Cy5	JIR-712-175-153	donkey	1:500	histology, secondary
PTBP1	EPR9048B	rabbit	1:10’000	Western blot, primary
ACTB	ab8226	mouse	1:2’000	Western blot, primary
IRDye® 680RD anti-rabbit IgG	926-68073	donkey	1:20’000	Western blot, secondary
IRDye® 800CW anti-mouse IgG	926-32212	donkey	1:20’000	Western blot, secondary

Supplementary table 5: Oligos used for deep sequencing.

oligo name	sequence (5’ → 3’)
PTBP1.ex1-HTS_fwd	CTTTCCCTACACGACGCTCTTCCGATCTNNNNNNTTCTGCTATTCCTGCGCCTC
PTBP1.ex1-HTS_rev	GGAGTTCAGACGTGTGCTCTTCCGATCTNNNNNNCATTGCAGCGGTTAGAGGGA
PTBP1.ex3-HTS_fwd	CTTTCCCTACACGACGCTCTTCCGATCTNNNNNNTGCAAATGGGAATGCAGGAA
PTBP1.ex3-HTS_rev	GGAGTTCAGACGTGTGCTCTTCCGATCTNNNNNNCAGGTCCTTTCTCCCAGCTC
PTBP1.ex7.1-HTS_fwd	CTTTCCCTACACGACGCTCTTCCGATCTNNNNNNATGCCAAGCTGGTGAGTAGG
PTBP1.ex7.1-HTS_rev	GGAGTTCAGACGTGTGCTCTTCCGATCTNNNNNNGCAGGTCAGGTCGAGTGTAG
PTBP1.ex7.2-HTS_fwd	CTTTCCCTACACGACGCTCTTCCGATCTNNNNNNCTACACTCGACCTGACCTGC
PTBP1.ex7.2-HTS_rev	GGAGTTCAGACGTGTGCTCTTCCGATCTNNNNNNATCACTGCACCTCACCTCAC
PTBP1.ex8-HTS_fwd	CTTTCCCTACACGACGCTCTTCCGATCTNNNNNNGTCAGCCTCTCCGTATGCAG
PTBP1.ex8-HTS_rev	GGAGTTCAGACGTGTGCTCTTCCGATCTNNNNNNCCTGTGGATGCTTCTGGAGG
PTBP1.ex9-HTS_fwd	CTTTCCCTACACGACGCTCTTCCGATCTNNNNNNGGTGCTGGGAATTCTGTCCT
PTBP1.ex9-HTS_rev	GGAGTTCAGACGTGTGCTCTTCCGATCTNNNNNNCAGCAGTGGCAGATAGAGGG
Mypn1_HTS_fwd	CTTTCCCTACACGACGCTCTTCCGATCTNNNNNNGGTCAAAAATGGCGCAAGGT
Mypn1_HTS_rev	GGAGTTCAGACGTGTGCTCTTCCGATCTNNNNNNTGCACACACTGACAAGGACT
Ank1_HTS_fwd	CTTTCCCTACACGACGCTCTTCCGATCTNNNNNNTGTTTTCTGCTTCTCAGGGGA
Ank1_HTS_rev	GGAGTTCAGACGTGTGCTCTTCCGATCTNNNNNNCAGTGGTCCAAGACCGTACA

Supplementary table 6: Reference nucleotide sequences of amplicons for deep sequencing.

amplicon name	amplicon sequence (5’→ 3’)
PTBP1.ex1	TTCTGCTATTCCTGCGCCTCCGCTCCGTTCCCCGCGGGTCTCTTCCGTGTGCCATGGA CGGGTAAGTCCTGCCGCGCCCCTCGCACGCCGCTCCGCTCACCACTCCGTCCCAGCCA TCGCTGCCGCGCGCGTGGACTTTTGGCCCCCGCCGATCCCTCTAACCGCTGCAATG
PTBP1.ex3	TGCAAATGGGAATGCAGGAAAGGAATCAGCCTGGAACTAAGATTCCATGCTCTCTTCT CAGCGGGGATCCGACGAGCTCTTCTCCACGTGTGTCAGCAACGGCCCCTTCATCATGA GCAGCTCTGCCTCAGCAGGTAAGAGTGCCTGGGTGCCCTAGGGAGTCCTGCCTTGACA GGTACAGGGCGAGCTGGGAGAAAGGACCTG
PTBP1.ex7.1	ATGCCAAGCTGGTGAGTAGGACTTGCTTGGGTGGGCAATCCTATGACTGGCCCACGCA CTCACCTATGGCTCCCCACAGTCCCTGGATGGCCAGAACATCTACAACGCCTGCTGCA CGCTGCGCATCGACTTCTCCAAGCTCACCAGTCTCAATGTCAAGTACAACAATGATAA GAGCAGAGACTACACTCGACCTGACCTGC
PTBP1.ex7.2	CTACACTCGACCTGACCTGCCCTCTGGAGACAGCCAGCCTTCACTAGACCAGACCATG GCAGCAGCCTTTGGTAAGATGCTGTACTGAGACACACCAAATGAACAGGGGTGGGACA GGCCACCTAGCTGTCAGGGCACCCTGGCACTGCACAGCCCAGCCACTCAGCAGTCCTG CCCGTGCCTGGCCCAGCCGTGAGGTGAGGTGCAGTGAT
PTBP1.ex8	GTCAGCCTCTCCGTATGCAGGAGCCGGGTTCCCTCCCACCTTTGCCATCCCTCAGGCC GCAGGTATTCACGCTCATCCTGACCCCAGCGCCTGCATGCCCACACAGCCCCATAACT GTCCATAGACCGGGATGCCACTGGCCCCAAGTGTTAGGCCCCAGGCCCCCTTCCTTCT GGGGAGAGGGGAAGGGGCCTCCAGAAGCATCCACAGG
PTBP1.ex9	GGTGCTGGGAATTCTGTCCTTTTGGTCAGCAATCTGAACCCTGAGGTATGTGGGTATT GCTGTGCTCTGCTTATACATGGAGTAGTGGTGGGGTGCTGACTGACCACAAGTCAGGG TGGGGGAGCATACTGGATGGCAAGCAGGGTTTCTGGGTGTCCCAGGCGCCGTGTGGGT ATAGGCGTGCTGCCCCTCTATCTGCCACTGCTG

amplicon name	amplicon sequence (5′→ 3′)
Mypn-OT1	GGTCAAAAATGGCGCAAGGTCAGAGGGCACCGTGGGTTCCAGCACACCTGCCCGCAGC GCTTCATCCATAGGCCCTGAGCTACCACCCAGCTCTGCTTCAGCAGGTACCCAGTACA GCTTGAGGTCAGCAGCTTGCTCCCATGCCTGTTCTTTGCTTTGCAAATGAGTCCTTGT CAGTGTGTGCA
Ank1-OT2	TGTTTTCTGCTTCTCAGGGGAGAATCAGCTGTTCTGGCCATTTGATGGTACAGGGTTT GCCCATTCGAAGCCGACTCAGCCCTGCTCTGTCTCACAGGTAAGCACACGAGATCCCC CTTTTCTGGAGCCCTCCAGCGACCCCACTCACCACAGTGAACAGAAGTTGTACGGTCT TGGACCACTG

1364

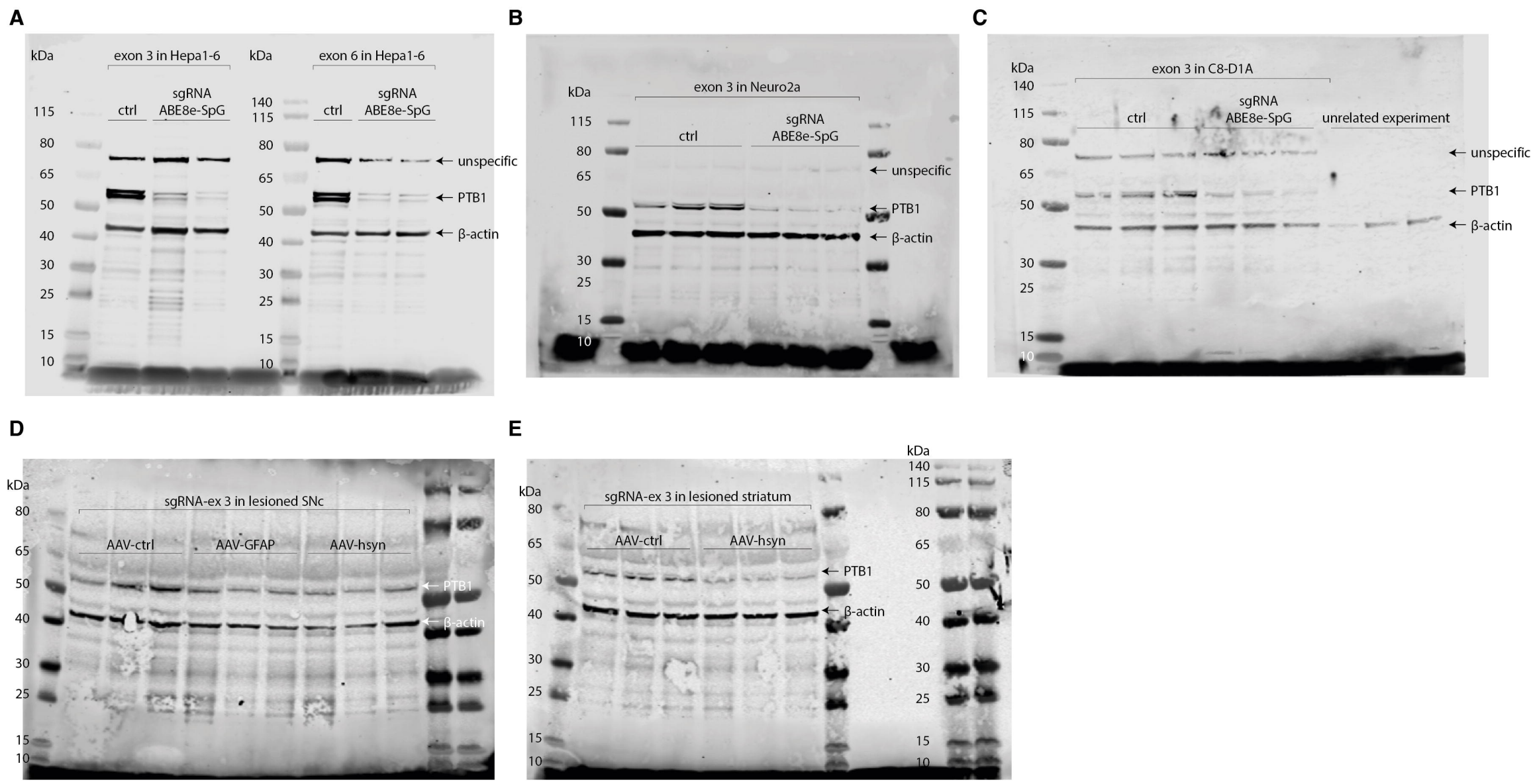
A
kDa
exon 3 in Hepa1-6
ctrl
sgRNA ABE8e-SpG
115
80
65
50
40
30
25
15
10
kDa
exon 6 in Hepa1-6
ctrl
sgRNA ABE8e-SpG
140
115
80
65
50
40
30
25
15
10
unspecific
PTB1
β-actin
B
kDa
exon 3 in Neuro2a
ctrl
sgRNA ABE8e-SpG
115
80
65
50
30
25
15
10
unspecific
PTB1
β-actin
C
kDa
exon 3 in C8-D1A
ctrl
sgRNA ABE8e-SpG
unrelated experiment
140
115
80
65
50
30
25
15
10
unspecific
PTB1
β-actin
D
kDa
sgRNA-ex 3 in lesioned SNc
AAV-ctrl
AAV-GFAP
AAV-hsyn
80
65
50
40
30
25
15
10
PTB1
β-actin
E
kDa
sgRNA-ex 3 in lesioned striatum
AAV-ctrl
AAV-hsyn
80
65
50
40
30
25
15
10
PTB1
β-actin
kDa
140
115
80
65
50
40
30
25
15
10